

# Solvent Effects on the Physicochemical Properties of the Cross-Linked Histidine–Tyrosine Ligand of Cytochrome *c* Oxidase

William J. McDonald\* and Ólöf Einarsdóttir

Department of Chemistry and Biochemistry, University of California, Santa Cruz, California 95064

Received: October 6, 2009; Revised Manuscript Received: February 4, 2010

Density functional theory was used to explore the effects of aqueous solvation on the structure, vibrational frequencies, and the electronic absorption spectrum of 2-(4-methylimidazol-1-yl)-phenol (Me-ImPhOH), a chemical analogue of the cross-linked histidine–tyrosine Cu<sub>B</sub> ligand of cytochrome *c* oxidase. In addition, the phenolic–OH p*K*<sub>a</sub>, the anodic redox potential for the biring radical/anion couple, and the phenolic–OH bond dissociation energy were calculated relative to phenol using a series of isodesmic reactions. In the gas phase, the imidazole moiety stabilizes the biring anion for all the models and greatly decreases the phenolic–OH p*K*<sub>a</sub> relative to phenol. Moreover, the conductor-like polarizable continuum model (C-PCM)-water-solvated reactions predict Δp*K*<sub>a</sub> values that are five times smaller than the gas-phase reactions, in agreement with the proposed role of the cross-linked histidine–tyrosine as a proton donor in the enzyme. For the neutral biring radical solvation models, the imidazole moiety induces a high degree of asymmetry into the phenol ring when compared to unmodified phenoxy radical. The biring radical π-bonds of the imidazole ring are more localized when compared to unmodified 1-methylimidazole and Me-ImPhOH solvation models, suggesting reduced aromaticity for all biring radical solvation models. The C-PCM-water-solvated reactions predict relative biring radical reduction potentials that are an order of magnitude smaller than the gas-phase reactions. The biring O–H bond is weakened relative to phenol by less than 4 kcal/mol for all the reactions studied, suggesting that the imidazole moiety does not facilitate H-atom abstraction in the enzyme. Together, these results demonstrate the sensitive nature of the proton and electron donating ability of the histidine–tyrosine cross-linked ligand in cytochrome *c* oxidase and suggest that for quantitative predictions of reaction energies and thermodynamic properties, models of this ligand should take care to account for changes in environment and, more specifically, hydrogen bonding interactions.

Cytochrome *c* oxidase (CcO; see the Abbreviations paragraph for all abbreviations herein) catalyzes the four-electron reduction of dioxygen to water,<sup>1</sup> and couples this reaction to the translocation of protons across the inner mitochondrial (or bacterial plasma) membrane, thereby providing the electrochemical proton gradient necessary for ATP synthesis.<sup>2</sup> The O<sub>2</sub> reduction reaction occurs at the heme *a*<sub>3</sub>/Cu<sub>B</sub> binuclear center. X-ray crystallographic studies of the bovine enzyme<sup>3,4</sup> have identified a highly conserved, covalent cross-link between the C5' of a tyrosine residue (Y244 in the bovine numbering) and the ε-nitrogen of histidine 240, a ligand to Cu<sub>B</sub> (Figure 1).<sup>5</sup> Under steady-state reaction conditions, where electron flux through Cu<sub>A</sub> and heme *a* into the *a*<sub>3</sub>/Cu<sub>B</sub> binuclear center is rate limiting,<sup>6,7</sup> two of the four electrons required to reduce O<sub>2</sub> to H<sub>2</sub>O are contributed by the high-spin heme *a*<sub>3</sub>. The mono-nuclear Cu<sub>B</sub> center contributes one electron, and the cross-linked tyrosine has been proposed to contribute the fourth electron<sup>8,9</sup> as well as a proton,<sup>10,11</sup> generating a neutral tyrosyl radical. The physicochemical properties relevant to the electron and proton donating ability of the histidine–tyrosine (H–Y) ligand are the redox potential for the ground-state/tyrosyl radical couple and the phenolic p*K*<sub>a</sub>, respectively. In addition, the optical absorption and vibrational spectra of the singlet and radical states are expected to be diagnostic of the generation of a tyrosyl radical.

Whereas early experiments<sup>8,9</sup> have provided support for the existence of a tyrosyl radical during CcO enzymatic turnover,

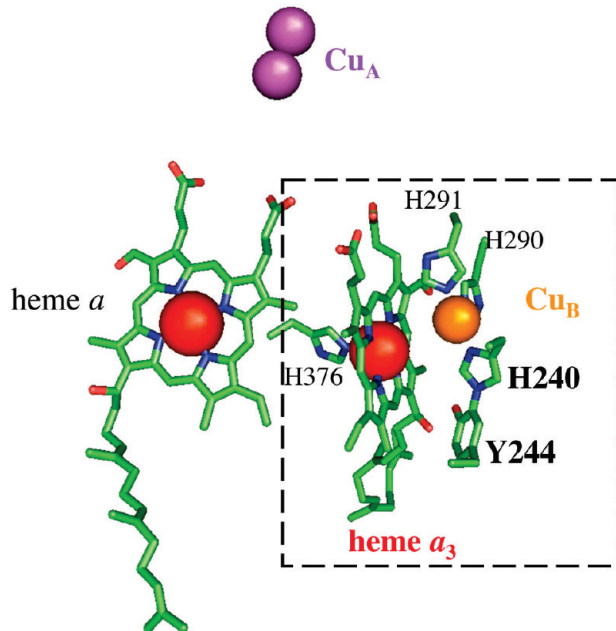


**Figure 1.** The redox-active metal centers of the bovine cytochrome *c* oxidase (pdb 2EIJ<sup>4</sup>): the *a*<sub>3</sub>/Cu<sub>B</sub> binuclear center is enclosed in the dashed box. The metal atoms appear as spheres, and the ligand atoms, as lines. Atom colors: Fe, red; Cu<sub>B</sub>, orange; Cu<sub>A</sub>, magenta; carbon, green; oxygen, red; nitrogen, blue. For clarity, hydrogen atoms are omitted. Graphic generated using PyMOL.<sup>5</sup>

\* To whom correspondence should be addressed. Telephone: (831) 459-3061. Fax: (831) 459-2934. E-mail: mcdonald@chemistry.ucsc.edu.

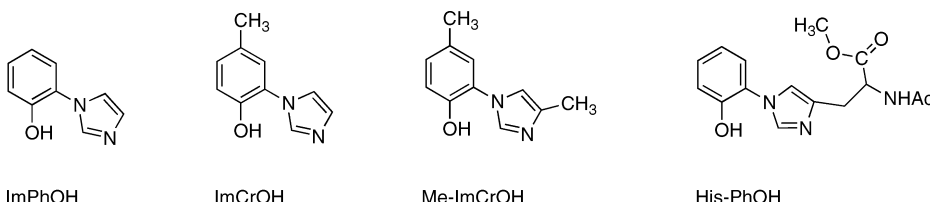


**Figure 2.** Chemical models of the cross-linked histidine–tyrosine ligand that have appeared in the literature.<sup>20–28</sup>

direct evidence is still lacking. For example, the reaction of CcO with  $H_2O_2^{12}$  produced an EPR signal that was attributed to the cross-linked tyrosyl radical. Further experiments, however, cast some doubt as to the origin of the  $g \approx 2$  signal,<sup>13</sup> suggesting that this reaction produces a tryptophan cation radical and a porphyrin cation radical<sup>14</sup> or an unmodified tyrosyl radical removed from the binuclear active site.<sup>15</sup> Furthermore, although vibrational spectroscopy has been used to identify nuclear motions and structural changes associated with the generation of tyrosyl radicals in enzymes,<sup>16</sup> the definitive assignment of spectral bands characteristic of a tyrosyl radical in CcO has been problematic.<sup>17–19</sup>

Because the direct measurement of the physicochemical properties for the H–Y ligand in the enzyme is inaccessible, several groups have synthesized chemical models that include the phenol–imidazole motif (Figure 2).<sup>20–26</sup> These include the imidazole–phenol biring<sup>20</sup> (ImPhOH) and the methylated homologues 2-(imidazol-1-yl)-4-methylphenol<sup>21,22</sup> (ImCrOH) and 2-(4-methylimidazol-1-yl)-4-methylphenol (Me-ImCrOH).<sup>23</sup> A cross-linked histidine–phenol (His-PhOH) has also been reported.<sup>24,25</sup> Experiments on these chemical models have shown that the oxidation potential of the imidazole–phenol moiety is 66–110 mV<sup>20,21,26</sup> more positive than that of unmodified tyrosine, and the biring phenolic  $pK_a$  is downshifted 1.1–1.8 log units when compared to tyrosine,<sup>20–22,28</sup> in agreement with the proposed role of H–Y as a proton donor. Furthermore, time-resolved optical absorption experiments have identified a unique band at  $\sim 500$  nm characteristic of the cross-linked histidine–phenoxy radical (His-PhO $^\bullet$ ) that is not observed in the spectrum of the unmodified tyrosyl radical or in the spectrum of the histidine–tyrosyl radical dipeptide;<sup>25</sup> this unique absorption is 100 nm to the red of the 400 nm absorption attributed to the unmodified tyrosyl radical.<sup>25</sup>

In complement to experiments on chemical models, computation has provided a deeper understanding of the unique properties of the histidine–tyrosine ligand.<sup>20,23,27–29</sup> The van der Donk group<sup>20</sup> used the B3LYP hybrid density functional combined with the COSMO polarized continuum solvent model<sup>27</sup> to calculate the effects of the covalent cross-link on the phenolic  $pK_a$ , the oxidation potential, and the O–H bond dissociation energy of ImPhOH. Bu and Cukier<sup>28</sup> used the B3LYP hybrid density functional with the Me-ImCrOH model to investigate the gas-phase proton and electron transfer reactions that lead to radical generation. Kim et al.<sup>23</sup> calculated the EPR spectral parameters for Me-ImCrO $^\bullet$  at the B3LYP/6-311++G\*\* level, and Colbran and Paddon-Row<sup>29</sup> examined the energetic effects of the histidine–tyrosine cross-link on the proton-pumping ability of CcO at a level of theory similar to that used by Kim et al.<sup>23</sup>

In agreement with experiment,<sup>20,21,25</sup> computational studies on model compounds containing the cross-link have shown that the phenolic  $pK_a$  is lowered and the oxidation potential is more positive when compared to unmodified tyrosine.<sup>21,28</sup> While these and other<sup>23,30</sup> spectroscopic markers and important trends in the physicochemical properties of the histidine–tyrosine ligand have

been reproduced, it is not precisely known how such properties change upon going from the highly inhomogeneous low-dielectric environment of a membrane-bound enzyme to the high-dielectric aqueous environment. In addition, the effect of the environment on the electronic absorption spectra of the singlet and doublet states of the biring has not been investigated. It is therefore unclear how the results from experiments on model compounds obtained in aqueous solution or the results from gas-phase calculations compare to the largely unknown properties of the ligand in the enzyme.

In the present work, the effects of aqueous solvation on the physicochemical properties of the histidine–tyrosine biring ligand are explored using hybrid density functional theory and the 2-(4-methylimidazol-1-yl)-phenol (Me-ImPhOH) chemical model. The electrostatic and H-bonding solvent–solute interactions are explored independently by comparing calculated properties obtained with the conductor-like polarizable continuum model (C-PCM) of Barone and Cossi<sup>31,32</sup> alone and in combination with explicit water molecules H-bonded to the N $_\delta$  of imidazole and the phenolic oxygen. The properties investigated include the structure, the fundamental vibrational frequencies and the electronic absorption spectra for solvation models of the singlet neutral, singlet anion, and doublet radical states. In addition, the phenolic  $pK_a$ , the redox potential for the singlet anion/radical couple, and the phenolic O–H bond dissociation energy (BDE) are calculated relative to phenol and the phenoxy radical using an isodesmic reaction scheme. The results show that for the neutral biring radical solvation models, the imidazole moiety induces a high degree of asymmetry into the phenol ring when compared to unmodified phenoxy radical, and the  $\pi$ -bonds of the imidazole ring in the biring radicals are more localized when compared to unmodified 1-methylimidazole and Me-ImPhOH solvation models, suggesting reduced aromaticity for all radical biring solvation models. Both the shift in the phenolic  $pK_a$  of Me-ImPhOH relative to phenol and the reduction potential of the biring radical relative to phenoxy radical are strongly solvation-dependent, and these properties are 5–10 times smaller in the C-PCM-water than in the gas phase. For all reactions, the imidazole moiety increases the acidity of the phenolic O–H, supporting the proposed role of the biring ligand as a proton donor. The phenolic O–H BDE of the biring is less sensitive to solvation than the  $pK_a$  or the reduction potential of the radical; however, for all solvation models, the O–H bond of the biring ligand is weakened relative to phenol by less than 4 kcal/mol, suggesting that the imidazole moiety does not facilitate H-atom abstraction in the enzyme.

## Computational Method

All calculations were performed using the GAMESS<sup>33</sup> software suite. Unconstrained geometry optimizations and double-differenced seminumerical nuclear-Hessian calculations were performed at the (R,U)B3LYP<sup>34,35</sup>/6-31+G(d,p)<sup>36</sup> level of theory, where “(R,U)” indicates that the spin-restricted method was used for all closed-shell structures, and the spin-unrestricted

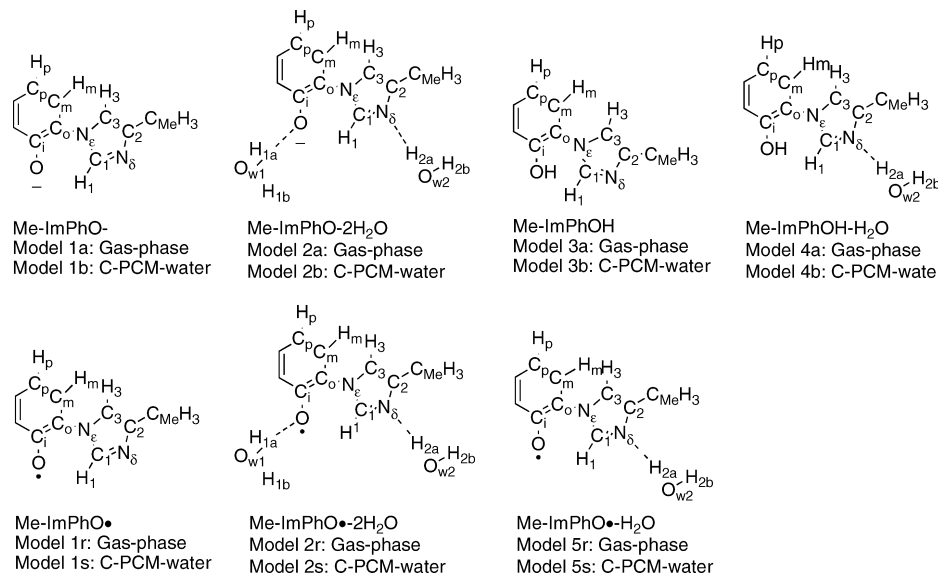


**Figure 3.** Atom label definitions for the computational models.

method was used for all open-shell structures. The C-PCM-water-solvated structures and vibrational frequencies were obtained with only the electrostatic solute–solvent interactions included in the solvation Hamiltonian. Time-dependent B3LYP (TDB3LYP) calculations were performed for gas-phase models at the (R,U)B3LYP/6-31+G(d,p) geometries using the def2TZVPP(+) basis set from the Ahlrichs group;<sup>37</sup> the “(+)” indicates that the s,p,d,f-diffuse functions from the aug-cc-pVTZ basis set<sup>38</sup> were added to all H-bonded heavy atoms, that is, the N<sub>δ</sub>-nitrogen of imidazole and the oxygen atoms of phenol and water (see Figure 3 for the solvation model atom label definitions).

The biring phenolic pK<sub>a</sub> was calculated relative to phenol using isodesmic reactions and the B3LYP/def2TZVPP(+)//B3LYP/6-31+G(d,p) energies. Reaction energies and the corresponding ΔpK<sub>a</sub> values were computed in the gas phase and in C-PCM-water. The only solute–solvent interactions included in the solvation energies were the self-consistent electrostatic energy. The unscaled B3LYP/6-31+G(d,p) zero-point energies were included in the reaction energies.

The reduction potential for the biring radical/anion couple was obtained relative to phenolate anion/phenoxyl radical using isodesmic reactions. Similarly, the phenolic O–H bond dissociation energy (BDE) for Me-ImPhOH was calculated relative to phenol using isodesmic reactions. The (R,U)B3LYP/def2TZVPP(+)//(R,U)B3LYP/6-31+G(d,p) reaction energies were computed in the gas phase and in C-PCM-water. Only the self-consistent electrostatic solute–solvent interaction energy was included in the solvated reaction energies, and the unscaled (R,U)B3LYP/6-31+G(d,p) zero-point energies were included in all of the reactions.

Because the B3LYP hybrid density functional is known to provide inconsistent results for weak interactions<sup>39,40</sup> and underbind H-bonded complexes,<sup>41</sup> all of the gas-phase and C-PCM reaction energies and corresponding thermodynamic quantities involving the H-bonded models 2a–b, 4a–b, 2r–s, and 5r–s (Figure 3) were repeated using the PBE0<sup>42</sup> hybrid density functional. Optimized geometries and nuclear-Hessian calculations were obtained at the (R,U)PBE0/6-31+G(d,p) level of theory, and reaction energies were computed at the stationary points using the def2TZVPP(+) basis set.

## Results

**Effects of Solvent on Structure. Singlet-State Models: Me-ImPhO<sup>−</sup> and Me-ImPhOH.** Selected structural parameters for Me-ImPhO<sup>−</sup> and Me-ImPhOH solvation models appear in Figure 4,<sup>43</sup> where the anionic solvation models 1a–2b appear in the upper image and the neutral models 3a–4b appear in the lower image. It is expected that for the anionic models, solvation will produce a significant structural change at the center of the negative charge (viz., the OC<sub>i</sub> stretch), and from Figure 4, it is clear that this is the case. Furthermore, solvation significantly shortens the long C<sub>0</sub>C<sub>i</sub> and C<sub>0</sub>'C<sub>i</sub> bonds of the gas-phase Me-ImPhO<sup>−</sup> (Figure 4, model 1a vs 2b). For the neutral structures, however, solvation most strongly perturbs the C<sub>1</sub>N<sub>e</sub> bond of imidazole (see Figure 3 for the atom label definitions), and in contrast to the anionic solvation models, the C<sub>0</sub>C<sub>i</sub> and C<sub>0</sub>'C<sub>i</sub> bonds of the neutral Me-ImPhOH do not change with solvation model, and except for the ~0.01 Å elongated C<sub>0</sub>C<sub>i</sub> bond observed for all the Me-ImPhOH solvation models 3a–4b, the CC bonds of the neutral phenol moiety do not differ significantly from those of an ideal benzene ring. It should also be noted that for both the anionic and neutral solvation models, solvation widens the C<sub>1</sub>N<sub>e</sub>C<sub>0</sub>C<sub>i</sub> torsion angle 11–12° (1a vs 2b and 3a vs 4b); however, the C<sub>1</sub>N<sub>e</sub>C<sub>0</sub>C<sub>i</sub> torsion angles of the neutral structures are consistently 15° wider than that of the corresponding anionic structure (e.g., 1a vs 3a and 2b vs 4b).

The calculated structures of the gas-phase models 1a and 3a can be compared to the gas-phase B3LYP/6-311++G\* calculations of Bu and Cukier,<sup>28</sup> which used the Me-ImCrOH chemical model. Although the Me-ImCrOH model of ref 28 differs from Me-ImPhOH by the CH<sub>3</sub> group at the C<sub>p</sub> of the phenol ring (Figures 2 and 3), this is not expected to alter the geometry of the phenol ring significantly.<sup>44</sup> When comparing the gas-phase Me-ImPhO<sup>−</sup> to Me-ImCrO<sup>−</sup>, the largest structural difference is the 0.006-Å-longer C<sub>0</sub>C<sub>i</sub> bond of the former structure (1.457 vs 1.451 Å for Me-ImPhO<sup>−</sup> and Me-ImCrO<sup>−</sup>, respectively).<sup>28</sup> The OC<sub>i</sub> bond is similarly 0.005 Å longer when comparing the same two structures (1.273 Å vs 1.268 Å, respectively).<sup>28</sup> For the gas-phase Me-ImPhOH and Me-ImCrOH, the largest structural difference is an increase of 0.006 Å in the C<sub>0</sub>'C<sub>i</sub> bond, where the Me-ImPhOH bond (1.398 Å) of the present investigation is longer than that of Me-ImCrOH (1.392 Å).<sup>28</sup> It should be noted

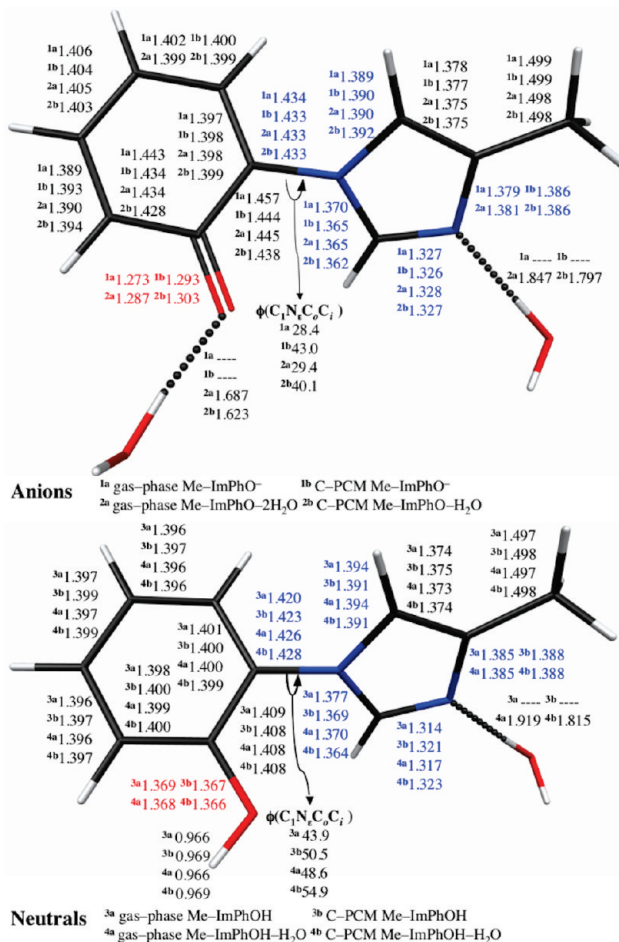


**Figure 4.** RB3LYP/6-31+G(d,p) calculated structural parameters (bond lengths in angstroms; torsion angle,  $\phi$ , in degrees) for anionic models 1a–2b (upper) and neutral models 3a–4b (lower). Generated using MacMolPlt 7.2.1.<sup>43</sup>

that the  $C_1N_eC_0C_i$  torsion angles for all calculated structures presented here are positive, whereas the gas-phase Me-ImCrO<sup>-</sup> and Me-ImCrOH torsion angles in ref 28 are  $-31^\circ$  and  $-45^\circ$  (cf.  $+28^\circ$  and  $+44^\circ$  in Figure 4), respectively.<sup>28</sup> However, at the RB3LYP/6-31+G(d,p) level of theory, there is no significant structural or energetic difference between the  $\pm\phi(C_1N_eC_0C_i)$  rotamers in the gas phase, nor is there any difference for the solvation models. Therefore, the differences between Me-ImPhOH and Me-ImCrOH may be an indicator of the precision of the calculated structural parameters.

The calculated Me-ImPhOH and Me-ImPhO<sup>-</sup> solvation model structures can also be compared to our recent calculations<sup>44</sup> of the solution structures of phenol and phenolate anion using the same methodology. When Me-ImPhO<sup>-</sup> is compared to phenolate anion solvation models, a 0.053 Å increase in the phenolic O $\cdots$ H<sub>1a</sub> H-bond distance is observed in the gas-phase Me-ImPhO-2H<sub>2</sub>O (1.687 Å) over that in the gas-phase phenolate-H<sub>2</sub>O complex (1.634 Å). A 0.018 Å increase is observed in the phenolic O $\cdots$ H<sub>1a</sub> H-bond distance for the C-PCM Me-ImPhO-2H<sub>2</sub>O over that in the C-PCM phenolate-H<sub>2</sub>O complex<sup>44</sup> (1.623 and 1.605 Å, respectively). Whereas the increased H-bonding distance in the gas phase and C-PCM Me-ImPhO-2H<sub>2</sub>O compared to the corresponding phenolate-H<sub>2</sub>O models suggests a weaker solute-solvent interaction and may indicate a greater delocalization of the negative charge into the phenol and imidazole rings, solvation produces a similar 0.035 and 0.030 Å increase in the OC<sub>i</sub> bond

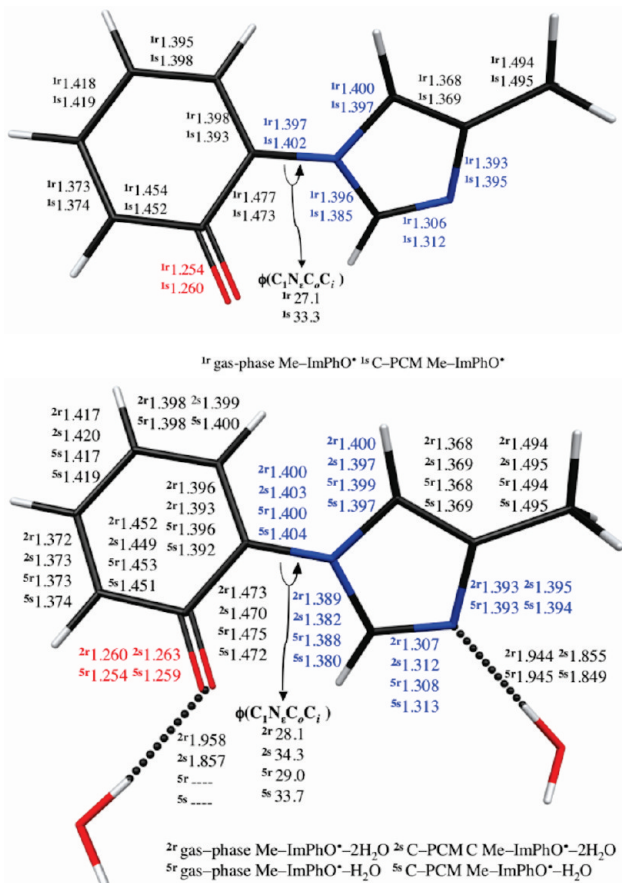


**Figure 5.** UB3LYP/6-31+G\*\* calculated structural parameters (bond lengths in angstroms; torsion angle,  $\phi$ , in degrees) for radical models 1r–2s, 5r–5s. Figure generated using MacMolPlt.<sup>36</sup>

when the gas-phase anions are compared to the C-PCM-water-solvated H-bonded complexes (1.276 vs 1.311 Å for phenolate and C-PCM phenolate-H<sub>2</sub>O, respectively,<sup>44</sup> and 1.273 vs 1.303 Å for Me-ImPhO<sup>-</sup> and C-PCM Me-ImPhO-2H<sub>2</sub>O, respectively). In addition, for all the Me-ImPhO<sup>-</sup> solvation models, the C<sub>0</sub>C<sub>i</sub> bond is 0.007–0.009 Å longer than in the corresponding phenolate anion solvation model.<sup>44</sup>

When comparing the Me-ImPhOH and phenol solvation models, the Me-ImPhOH solvation model C<sub>0</sub>C<sub>i</sub> bonds are 0.009 Å longer than in phenol<sup>44</sup> and C-PCM-water-solvated phenol. The consistent and charge-independent increase in the C<sub>0</sub>C<sub>i</sub> bond lengths for all solvated cross-linked models (cf. 0.007–0.009 Å for the Me-ImPhO<sup>-</sup> solvation models) over those observed in phenol and phenolate suggests that this increase is due to steric repulsion and is not an electronic effect. Furthermore, although the gas-phase Me-ImPhOH and gas-phase Me-ImCrOH<sup>28</sup> OC<sub>i</sub> bond is 0.004 Å shorter when compared to phenol and para-cresol, respectively, all remaining birning phenolic bonds are in close agreement with those of phenol<sup>44</sup> and para-cresol.<sup>28</sup> This structural similarity, combined with the wide C<sub>1</sub>N<sub>e</sub>C<sub>0</sub>C<sub>i</sub> torsion angle, suggests that for the neutral Me-ImPhOH solvation models, the imidazole and phenol  $\pi$ -electron systems are largely electronically uncoupled.

**Radical Models.** Selected structural parameters for the Me-ImPhO<sup>\*</sup> solvation models appear in Figure 5. It is expected that solvation will have a smaller impact on the structure of the neutral phenoxy radical moiety than on the charged phenolate anion, and this is, indeed, the case. Figure 5 shows that solvation lengthens the OC<sub>i</sub> bond 0.009 Å (models 1r vs 2s); this increase is considerably smaller than the 0.030 Å increase observed for

the Me-ImPhO<sup>−</sup> solvation models, but is larger than the insignificant 0.003 Å decrease in this bond length observed for the Me-ImPhOH solvation models. Furthermore, the radical solvation model OC<sub>i</sub> bonds are 0.01–0.04 Å shorter than the bonds of the corresponding anionic biring solvation models and are a consistent 0.11 Å shorter than in the corresponding singlet neutral biring solvation models suggesting a high degree of O–C double bond character. The C<sub>0</sub>C<sub>i</sub> bond for the gas-phase Me-ImPhO<sup>•</sup> (model 1r) is shortened when compared to the C-PCM-water-solvated Me-ImPhO<sup>•</sup>–2H<sub>2</sub>O (model 2s); however, the radical C<sub>0</sub>C<sub>i</sub> bonds are consistently 0.02–0.03 Å longer than the bonds of the corresponding anionic solvation model. The C<sub>0</sub>'C<sub>i</sub> radical bonds follow a similar trend: solvation shortens the radical C<sub>0</sub>'C<sub>i</sub> bond; however, the radical C<sub>0</sub>'C<sub>i</sub> bond is 0.02–0.03 Å longer than the bond of the respective anionic solvation model. It should be noted that for all the neutral radical solvation models, the C<sub>0</sub>C<sub>i</sub> bond is ~0.02 Å longer than the C<sub>0</sub>'C<sub>i</sub> bond of the same structure, reflecting a larger asymmetry in the C<sub>0</sub>C<sub>i</sub>/C<sub>0</sub>'C<sub>i</sub> bonds of the radical solvation models than in the ground-state anion and neutral solvation models.

Additional noteworthy structural features include the consistently short N<sub>e</sub>C<sub>0</sub> radical bond and narrow C<sub>1</sub>N<sub>e</sub>C<sub>0</sub>C<sub>i</sub> torsion angle. Furthermore, the C<sub>1</sub>N<sub>e</sub> bond length is shortened 0.016 Å and the N<sub>δ</sub>C<sub>1</sub> bond is lengthened 0.007 Å when the gas-phase Me-ImPhO<sup>•</sup> (model 1r) is compared to the C-PCM Me-ImPhO<sup>•</sup>–H<sub>2</sub>O (model 5s). This is similar to the 0.013 Å decrease and 0.009 Å increase in these two bonds, respectively, in the ground-state neutral structures (Figure 4, model 3a vs 4b). However, the C<sub>1</sub>N<sub>e</sub> bond length of the radical structures is ~0.02 Å longer and the N<sub>δ</sub>C<sub>1</sub> bond is ~0.01 Å shorter than in the corresponding ground-state neutral solvation models, which suggests increased localization of the π-bonds and a decrease in the aromaticity of the imidazole moiety for the radical biring structures.

The calculated gas-phase Me-ImPhO<sup>•</sup> (model 1r) geometry compares well with the gas-phase Me-ImCrO<sup>•</sup> calculation of ref 28. The gas-phase Me-ImPhO<sup>•</sup> (model 1r) OC<sub>i</sub> and C<sub>m</sub>'C<sub>0</sub>' bond lengths are predicted to be 0.008 Å longer than the corresponding bond lengths of the gas-phase Me-ImCrO<sup>•</sup>,<sup>28</sup> whereas all remaining equivalent bonds agree to within 0.005 Å. As with the ground-state neutral and anionic structures, the gas-phase Me-ImPhO<sup>•</sup> C<sub>1</sub>N<sub>e</sub>C<sub>0</sub>C<sub>i</sub> torsion angle is positive (+27°, Figure 5), and the torsion angle of ref 28 is −29°; however, at the UB3LYP/6-31+G(d,p) level of theory, there is no significant energetic or structural difference between the ±ϕ(C<sub>1</sub>N<sub>e</sub>C<sub>0</sub>C<sub>i</sub>) rotamers for the gas-phase model 1r or for the neutral radical solvation models.

The Me-ImPhO<sup>•</sup> solution structures can be compared to the calculated solution structure of the phenoxyl radical.<sup>44</sup> For the gas phase and C-PCM Me-ImPhO<sup>•</sup>–2H<sub>2</sub>O (models 2r–s), the phenolic O–H<sub>2</sub>O H-bond is 0.067 and 0.021 Å longer than the H-bond of the gas phase and C-PCM phenoxyl–H<sub>2</sub>O radical complexes, respectively.<sup>44</sup> Furthermore, for all the Me-ImPhO<sup>•</sup> solvation models, the OC<sub>i</sub> bond is, on average, 0.006 Å shorter than in the corresponding phenoxyl radical solvation model.<sup>44</sup> An additional interesting geometric difference between the Me-ImPhO<sup>•</sup> and phenoxyl radical solvation models is the structural asymmetry induced in the phenoxyl ring by the imidazole moiety. As with the C<sub>0</sub>C<sub>i</sub>/C<sub>0</sub>'C<sub>i</sub> bonds discussed above, the C<sub>m</sub>C<sub>0</sub> bonds are ~0.02 Å longer than the C<sub>m</sub>'C<sub>0</sub>' bonds of the same structure. Furthermore, the C<sub>m</sub>C<sub>0</sub> bonds are ~0.02 Å longer and the C<sub>m</sub>'C<sub>0</sub>' bonds are ~0.01 Å shorter in the Me-ImPhO<sup>•</sup> solvation models than the respective bonds in the corresponding phenoxyl radical solvation model.<sup>44</sup>

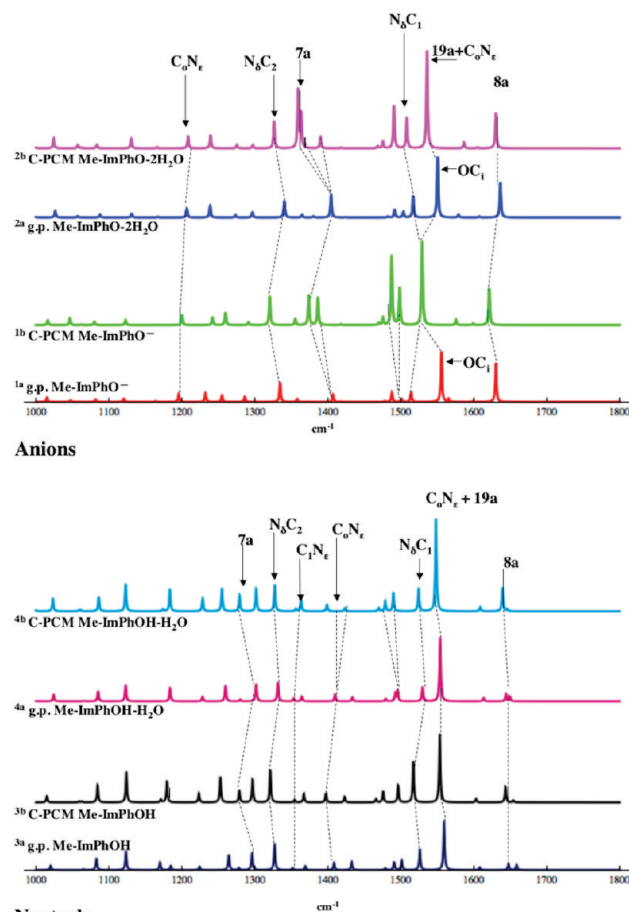


**Figure 6.** RB3LYP/6-31+G(d,p) calculated IR spectra for the anionic models 1a–2b (upper), and the neutral models 3a–4b (lower); g.p. = gas phase.

**Solvent Effects on the Infrared Spectra. Singlet-State Models: Me-ImPhO<sup>−</sup> and Me-ImPhOH.** The RB3LYP/6-31+G(d,p) calculated IR-absorbance spectra for the anionic solvation models 1a–2b and the neutral solvation models 3a–4b appear in Figure 6. Dashed lines are used to connect similar vibrational modes for the different solvation models. For structures with the same arrangement and number of atoms (i.e. the gas-phase and C-PCM-water-solvated pairs “a” and “b”, respectively), “similar” was determined quantitatively using vibrational projection analysis,<sup>45</sup> whereas for structures with differing numbers of atoms (e.g., the gas-phase Me-ImPhO<sup>−</sup> and Me-ImPhO–2H<sub>2</sub>O) “similar” is determined by comparing the total energy decomposition<sup>46</sup> of each normal mode, which has been projected onto a redundant set of primitive internal coordinates. In Figure 6, important vibrational modes are labeled with either the Wilson mode designation for the phenolic vibrational modes or the dominant primitive stretching coordinate. It must be emphasized that these Wilson mode abbreviations strictly apply to substituted benzene molecules in C<sub>2v</sub> point-group symmetry, and the labels in Figure 6 are used to simplify a comparison with a phenolate anion and phenol.

For the anionic biring solvation models 1a–2b, vibrations involving the OC<sub>i</sub> and the C<sub>0</sub>C<sub>i</sub>/C<sub>0</sub>'C<sub>i</sub> stretches are expected to be perturbed with inclusion of solvent, whereas for the neutral biring solvation models 3a–4b, the imidazole modes are expected to be sensitive to solvation. The phenol vibrational modes with large or solvation-dependent contributions of OC<sub>i</sub> stretching are Wilson modes 19a and 7a. We have recently proposed<sup>44</sup> an alternative criterion for distinguishing between

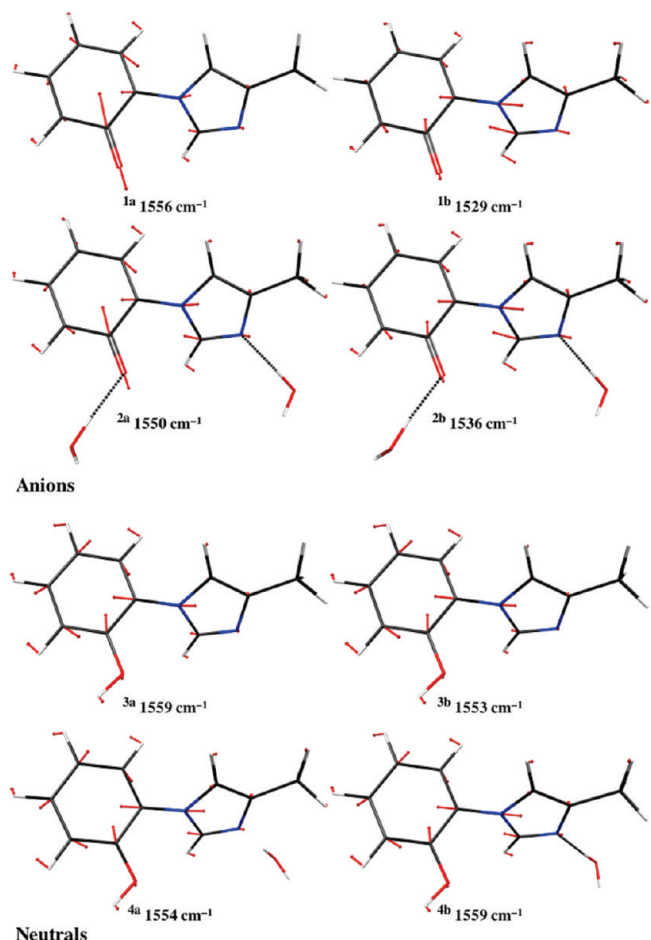


**Figure 7.** Calculated atomic displacements<sup>39</sup> for Wilson mode 19a.

these two modes on the basis of relative phasing of the  $\text{OC}_i$  and  $\text{C}_0\text{C}_i$  stretching motions, in which the Wilson mode 19a is an asymmetric combination of  $\text{OC}_i$  and  $\text{C}_0\text{C}_i$  stretching, and mode 7a is a symmetric combination of  $\text{OC}_i$  and  $\text{C}_0\text{C}_i$  stretching. The assignment of the Wilson modes 19a and 7a for the biring structures is based on the symmetric or asymmetric phasing of the  $\text{OC}_i$  and  $\text{C}_0\text{C}_i/\text{C}_0'\text{C}_i$  stretches.

**1500–1560 cm<sup>-1</sup> and  $\nu_{19a}$ .** For the phenolate anion solvation models and phenol, Wilson mode 19a is predicted near

1500–1550 cm<sup>-1</sup> and is largely CH bending motions, with contributions from phenolic CC stretching and solvation-dependent contributions of  $\text{OC}_i$  stretching.<sup>44</sup> For the gas-phase Me-ImPhO<sup>-</sup> and gas-phase Me-ImPhO-2H<sub>2</sub>O, the intense bands at 1555 and 1550 cm<sup>-1</sup>, respectively, have the same asymmetric combination of  $\text{OC}_i$  and  $\text{C}_0\text{C}_i/\text{C}_0'\text{C}_i$  stretching as is observed with phenolate anion (Figure 7). From the total energy decomposition of the anionic 1500 cm<sup>-1</sup> bands in Table 1A, it is clear that for the anionic solvation models, the  $\text{OC}_i$  stretch makes a significant contribution to the total energy of modes near 1500 cm<sup>-1</sup>. However, upon inclusion of solvent, the total energy contributed by the  $\text{OC}_i$  stretch is decreased, and furthermore, the energy of the mode with the largest  $\text{OC}_i$  stretching contribution is decreased. This is in agreement with the lengthening and weakening of the  $\text{OC}_i$  bond for the biring anions as solvation is included and is reflected in the intrinsic  $\text{OC}_i$  stretching frequencies<sup>47</sup> of 1431, 1386, 1326, and 1301 cm<sup>-1</sup> for the gas-phase Me-ImPhO<sup>-</sup> (model 1a), gas-phase Me-ImPhO-2H<sub>2</sub>O (model 2a), C-PCM Me-ImPhO<sup>-</sup> (model 1b), and C-PCM Me-ImPhO-2H<sub>2</sub>O (model 2b), respectively.

As is observed with phenol<sup>44</sup> and C-PCM-water-solvated phenol, the  $\text{OC}_i$  stretch contributes little energy to the intense Wilson mode 19a at 1550–1560 cm<sup>-1</sup>, and for all Me-ImPhOH solvation models, this stretch contributes less than 5% of the total energy (Table 1B). For the neutral models 3a–4b as well as the C-PCM-water-solvated anionic models 1b and 2b, the  $\text{N}_e\text{C}_0$  stretch contributes 10–12% of the total energy to the high-energy modes. By contrast, the  $\text{N}_e\text{C}_0$  stretch contributes only 4 and 6% of the total energy to the modes of the gas-phase anion models 1a and 2a, respectively (Table 1A).

The calculated frequencies for the gas-phase Me-ImPhO<sup>-</sup> and gas-phase Me-ImPhOH are in good agreement with the calculations of ref 28. For the gas-phase Me-ImCrO<sup>-</sup>, an intense absorption is predicted at 1556.4 cm<sup>-1</sup> (cf. 1556 cm<sup>-1</sup> for model 1a in Table 1A), which is described as C–O stretching.<sup>28</sup> For the gas-phase Me-ImCrOH, an intense frequency appears at 1557.3 cm<sup>-1</sup> (cf. 1559 cm<sup>-1</sup> for model 3a in Table 1B), which is described as C–N stretching.<sup>28</sup> The frequencies for models 1a and 3a in Table 1A and B, respectively, agree with those of ref 28. However, the energy contributed by individual primitive coordinates, such as the  $\text{OC}_i$  and  $\text{N}_e\text{C}_0$  stretches to the high-energy anionic 1530–1556 cm<sup>-1</sup> modes, is strongly solvation-dependent. From Table 1A and B, the total energy contributed

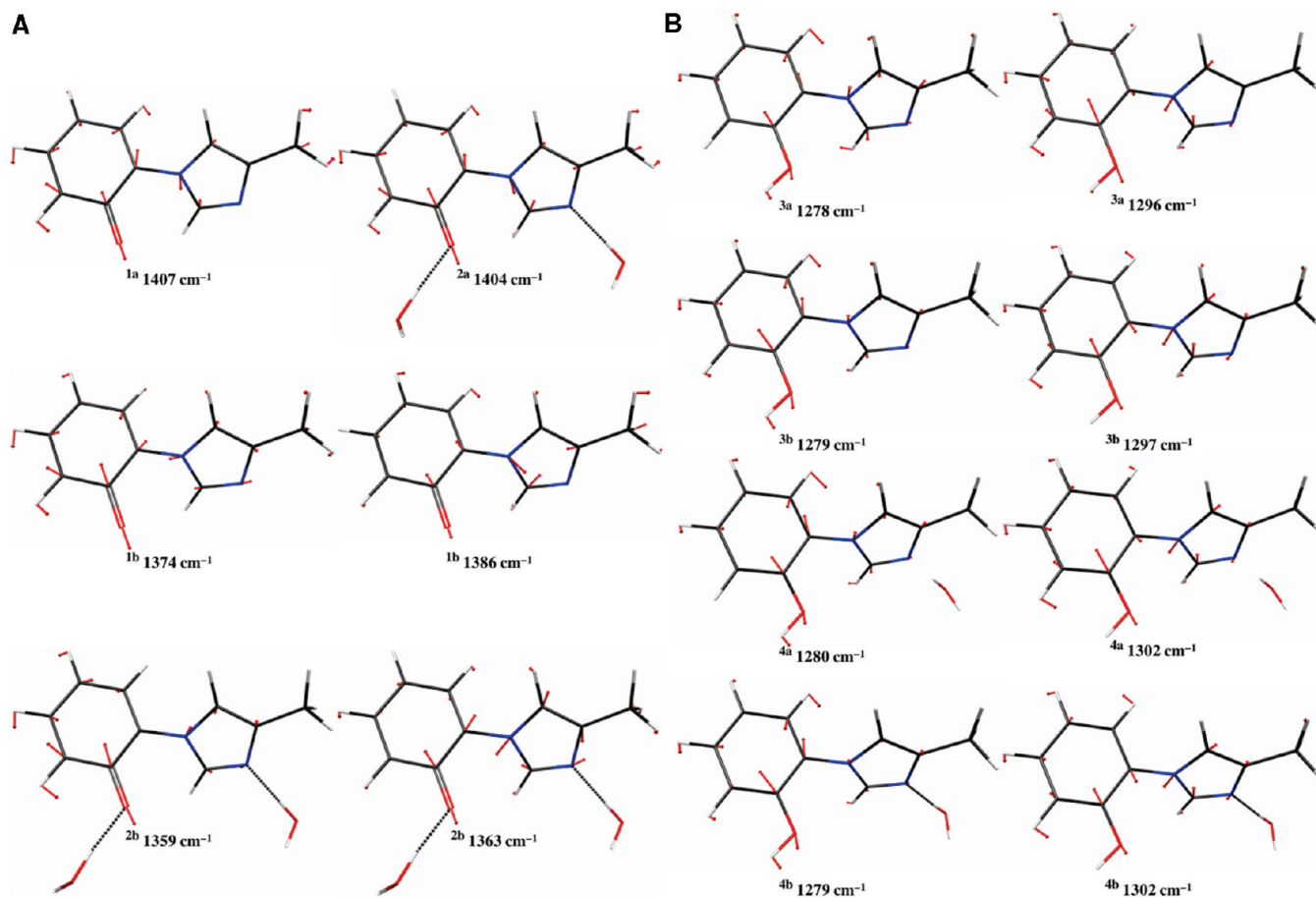
**TABLE 1**

(A) Total Energy Distribution (%) for Anionic Vibrational Frequencies Near 1500 cm <sup>-1</sup>												
model	1a			1b			2a			2b		
$\nu$ (cm <sup>-1</sup> )	1501	1514	1556	1488	1498	1529	1503	1517	1550	1491	1508	1536
$E$ (Im) <sup>a</sup>	5.4	45.5	9.8	3.6	22.2	59.3	4.4	45.6	22.7	4.4	33.8	49.3
$E$ (PhO <sup>-</sup> ) <sup>b</sup>	81.0	17.4	83.8	85.0	67.7	22.9	87.5	27.0	66.9	86.0	58.2	33.6
$E$ ( $\text{OC}_i$ ) <sup>c</sup>	1.9	8.6	40.6	20.4	4.9	4.4	5.8	10.5	23.0	11.5	4.4	4.7
$E$ ( $\text{N}_e\text{C}_0$ ) <sup>d</sup>	3.4	3.8	4.0	1.9	1.4	9.8	3.7	1.2	6.5	2.5	0.2	10.4
$E$ ( $\text{CH}_3$ ) <sup>e</sup>	8.1	30.9	0.7	4.1	7.8	5.6	0.8	23.2	1.9	1.4	5.8	3.7

(B) Total Energy Distribution (%) for Neutral Vibrational Frequencies Near 1500 cm <sup>-1</sup>												
model	3a			3b			4a			4b		
$\nu$ (cm <sup>-1</sup> )	1501	1526	1559	1497	1517	1553	1496	1530	1554	1501	1526	1559
$E$ (Im) <sup>a</sup>	3.2	78.2	8.5	2.7	78.0	8.0	6.8	65.6	21.7	4.0	62.9	23.7
$E$ (PhOH) <sup>b</sup>	82.4	12.2	78.7	89.6	11.0	80.3	47.8	26.0	62.9	88.2	29.6	61.3
$E$ ( $\text{OC}_i$ ) <sup>c</sup>	4.0	0.1	4.8	3.9	0.2	4.2	2.1	1.3	4.2	3.6	1.4	3.5
$E$ ( $\text{N}_e\text{C}_0$ ) <sup>d</sup>	1.9	0.4	11.0	1.6	1.5	10.2	1.2	0.0	12.3	1.9	0.2	11.9
$E$ ( $\text{CH}_3$ ) <sup>e</sup>	7.4	7.1	0.6	0.9	7.4	0.6	40.9	6.0	1.4	0.8	4.8	1.4

<sup>a</sup> The total energy contributed by imidazole. <sup>b</sup> The total energy contributed by phenolate (part A) or phenol (part B). <sup>c</sup> The energy contributed by the  $\text{OC}_i$  stretch. <sup>d</sup> The energy contributed by the  $\text{N}_e\text{C}_0$  stretch. <sup>e</sup> The energy contributed by the methyl group of imidazole.



**Figure 8.** (A) Calculated atomic displacements<sup>39</sup> for the anionic OC<sub>i</sub> stretching modes 7a. (B) Calculated atomic displacements<sup>39</sup> for the singlet neutral OC<sub>i</sub> stretching modes 7a.

by the phenolate moiety (Table 1A,  $E(\text{PhO}^-)$ ) decreases from 84% for the gas-phase Me-ImPhO<sup>-</sup> (model 1a) to 34% for the C-PCM Me-ImPhO-2H<sub>2</sub>O (model 2b), and the nuclear motions of the phenol ring (Table 1B,  $E(\text{PhOH})$ ) decrease from ~80 to 61% of the total energy for the ~1560 cm<sup>-1</sup> modes of the corresponding neutral Me-ImPhOH models 3a and 4b. In addition, for the anionic models 1a–2b, the N<sub>e</sub>C<sub>0</sub> stretching contribution is increased with inclusion of solvent, and for the C-PCM-solvated Me-ImPhO-2H<sub>2</sub>O (model 2b), the OC<sub>i</sub> and N<sub>e</sub>C<sub>0</sub> stretches make a contribution to the total energy of the 1536 cm<sup>-1</sup> mode similar to that in the neutral Me-ImPhOH solvation models. Furthermore, for the C-PCM-solvated anionic models 1b and 2b, the N<sub>d</sub>C<sub>1</sub> stretch contributes 16 and 13%, respectively (data not shown), of the total energy to mode 19a, whereas for the C-PCM-solvated neutral models 3b and 4b, this stretch contributes only 0.6 and 4%, respectively, of the total energy. These results are illustrated in Figure 7, where the calculated atomic displacements<sup>36</sup> for the anionic and neutral Wilson mode 19a are presented.

**1280–1420 cm<sup>-1</sup>,  $\nu_{7a}$ .** The phenolate anion solvation model Wilson mode 7a is predicted to be in the range of 1337–1400 cm<sup>-1</sup>, whereas for the phenol solvation models, mode 7a is predicted to be at 1265–1280 cm<sup>-1</sup>.<sup>44</sup> Despite the large variation in calculated frequencies, mode 7a is dominated by OC<sub>i</sub> stretching for all the anionic and neutral phenol solvation models, with variable contributions of phenolic CH bending and CC stretching.<sup>44</sup> The calculated Wilson mode 7a of the biring structures is in the range of 1360–1407 cm<sup>-1</sup> for the anionic solvation models 1a–2b and at 1280–1300 cm<sup>-1</sup> for the neutral solvation models 3a–4b, slightly blue-shifted when compared

to the phenolate anion solvation models and phenol.<sup>44</sup> This is in agreement with the shorter OC<sub>i</sub> bond lengths predicted for the biring structures. For the C-PCM-water-solvated anionic models 1b and 2b and all the neutral solvation models 3a–4b, the OC<sub>i</sub> stretch contributes to two modes, which are separated by 12 cm<sup>-1</sup> for the C-PCM-water-solvated anionic model 1b, 4 cm<sup>-1</sup> for model 2b, and 18–22 cm<sup>-1</sup> for the neutral models 3a–4b. From the calculated atomic displacements of Figure 8A and B, the Wilson mode 7a combines with the imidazole ring deformation modes, resulting in the observed splitting of the OC<sub>i</sub> stretch for the C-PCM-water-solvated anionic and all the neutral biring solvation models.

From the calculated atomic displacements in Figure 8A and B, it is clear that the 1407 cm<sup>-1</sup> gas-phase Me-ImPhO<sup>-</sup> mode and the 1404 cm<sup>-1</sup> gas-phase Me-ImPhO-2H<sub>2</sub>O mode have the same symmetric combination of OC<sub>i</sub> and C<sub>0</sub>C<sub>i</sub>/C<sub>0</sub>'C<sub>i</sub>' stretching as observed with the phenolate anion solvation models.<sup>44</sup> From the total energy decomposition data of Table 2A and B, the 1374 cm<sup>-1</sup> mode of the C-PCM-solvated model 1b has a larger OC<sub>i</sub> stretching contribution than the 1386 cm<sup>-1</sup> mode, and the model 1b 1374 cm<sup>-1</sup> mode has the same symmetric combination of OC<sub>i</sub> and C<sub>0</sub>C<sub>i</sub>/C<sub>0</sub>'C<sub>i</sub>' stretching as observed with the gas-phase models 1a and 2a and the phenolate anion (Figure 8A).<sup>44</sup> From Table 2A, the C-PCM-solvated anionic model 2b 1359 cm<sup>-1</sup> mode has the larger energy contribution from the OC<sub>i</sub> stretching than the 1363 cm<sup>-1</sup> mode. Furthermore, as presented in Figure 8A, the 1359 cm<sup>-1</sup> mode has larger amplitude phenolic CH bending motions than the 1363 cm<sup>-1</sup> mode; however, the C<sub>0</sub>C<sub>i</sub>/C<sub>0</sub>'C<sub>i</sub>' stretching contributions, while maintaining the correct symmetric phasing, are now split, with

TABLE 2

(A) Total Energy Decomposition (%) for Anionic OC <sub>i</sub> Stretching Frequencies Near 1400 cm <sup>-1</sup>						
model	1a	1b	2a	2b		
$\nu$ (cm <sup>-1</sup> )	1407	1374	1386	1404	1359	1363
$E$ (Im) <sup>a</sup>	11.0	13.3	42.0	16.7	10.5	42.8
$E$ (PhO <sup>-</sup> ) <sup>b</sup>	70.1	78.3	27.0	67.6	86.4	42.1
$E$ (OC <sub>i</sub> ) <sup>c</sup>	18.9	36.0	10.9	29.5	30.4	21.5
$E$ (N <sub>e</sub> C <sub>0</sub> ) <sup>d</sup>	0.2	3.9	9.2	1.2	0.6	4.0
$E$ (CH <sub>3</sub> ) <sup>e</sup>	11.6	3.0	17.9	8.2	0.6	4.6

(B) Total Energy Decomposition (%) for Neutral OC<sub>i</sub> Stretching Frequencies Near 1300 cm<sup>-1</sup>

model	3a	3b	4a	4b
$\nu$ (cm <sup>-1</sup> )	1278	1296	1279	1297
$E$ (Im) <sup>a</sup>	31.6	26.1	11.8	42.6
$E$ (PhOH) <sup>b</sup>	62.5	68.9	86.0	49.7
$E$ (OC <sub>i</sub> ) <sup>c</sup>	15.3	31.1	29.9	14.5
$E$ (N <sub>e</sub> C <sub>0</sub> ) <sup>d</sup>	1.5	2.0	0.3	3.3
$E$ (CH <sub>3</sub> ) <sup>e</sup>	3.6	0.1	1.0	1.1
				1.8
				0.8
				1.3
				1.1

<sup>a</sup> The total energy contributed by imidazole. <sup>b</sup> The total energy contributed by phenolate (part A) or phenol (part B). <sup>c</sup> The energy contributed by the OC<sub>i</sub> stretch. <sup>d</sup> The energy contributed by the N<sub>e</sub>C<sub>0</sub> stretch. <sup>e</sup> The energy contributed by the methyl group of imidazole

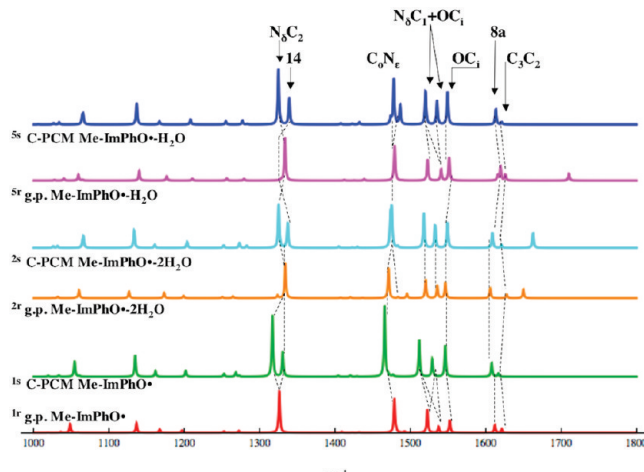


Figure 9. UB3LYP/6-31+G(d,p)-calculated IR spectra for the neutral radical solvation models 1r–2s, 5r–5s.

the C<sub>0</sub>C<sub>i</sub> stretch contributing to the 1363 cm<sup>-1</sup> mode and the C<sub>0</sub>'C<sub>i</sub> stretch contributing to the 1359 cm<sup>-1</sup> mode, reflecting the reduction of symmetry induced in the phenol ring by the N<sub>e</sub>C<sub>0</sub> bond.

From Table 2B, the higher-energy 1296 cm<sup>-1</sup> gas-phase Me-ImPhOH (model 3a) mode and the 1302 cm<sup>-1</sup> gas-phase Me-ImPhOH-H<sub>2</sub>O (model 4a) mode have the larger OC<sub>i</sub> stretching contribution, whereas for the C-PCM-water-solvated neutral models 3b and 4b, the lower energy modes at 1279 cm<sup>-1</sup> have the larger OC<sub>i</sub> stretching contribution, similar to what is observed for the C-PCM-water-solvated anionic models 1b and 2b.

**Radical Models.** The UB3LYP/6-31+G(d,p)-calculated IR-absorbance spectra of the Me-ImPhO<sup>•</sup> solvation models appear in Figure 9. As with the singlet-state neutral and anionic solvation models, important vibrational modes have been labeled with the Wilson mode designation for the phenolic vibrational modes or the dominant primitive stretching coordinate, and broken lines are used to connect similar vibrations across the different solvation models. For models with the same number and arrangement of atoms (i.e. the gas-phase and C-PCM radical pairs “r” and “s”, respectively), “similar” is determined quantitatively using vibrational projection analysis,<sup>45</sup> but for models with differing numbers of atoms, “similar” is determined by

comparing the total energy decomposition<sup>46</sup> of each mode, which has been projected onto a redundant set of primitive internal coordinates.

**1512–1523 cm<sup>-1</sup>, ν<sub>19a</sub>.** The neutral biring radical OC<sub>i</sub> stretch contributes to more than one vibrational frequency, as is observed with the C-PCM-water-solvated anions and all the singlet-state neutral solvation models. Consistent with the short OC<sub>i</sub> bond lengths predicted for all radical solvation models, this stretch contributes to frequencies >1500 cm<sup>-1</sup> (Table 3). Furthermore, in agreement with the short and solvent-sensitive N<sub>e</sub>C<sub>1</sub> bond, this stretch contributes to two high-energy frequencies. The N<sub>e</sub>C<sub>0</sub> stretch, by contrast, does not mix with the high-energy mode 19a as it does with the singlet-state models (Figure 6, Table 1A and B), but makes the largest energy contribution to frequencies near 1466–1487 cm<sup>-1</sup> (Figure 9, Table 3). The red shift in the N<sub>e</sub>C<sub>0</sub> stretch upon radical formation is not in agreement with the shorter bond length predicted for the radical solvation models and may be due to the decrease in aromaticity<sup>28</sup> discussed above.

The calculated frequencies can be compared to our recent calculations on the phenoxy radical solvation models.<sup>44</sup> The calculated gas-phase phenoxy radical OC<sub>i</sub> stretching frequency at 1489 cm<sup>-1</sup> is blue-shifted 28 cm<sup>-1</sup> with the inclusion of solvent.<sup>44</sup> From the total energy decomposition analysis in Table 3, the Me-ImPhO<sup>•</sup> solvation model OC<sub>i</sub> stretch makes the largest energy contribution to frequencies in the range of 1512–1524 cm<sup>-1</sup>, 33 cm<sup>-1</sup> higher than the corresponding phenoxy radical solvation model<sup>44</sup> and in agreement with the shorter biring OC<sub>i</sub> bond lengths. However, the Me-ImPhO<sup>•</sup> solvation model OC<sub>i</sub> stretching frequencies are less sensitive to solvation than in the unmodified phenoxy radical,<sup>44</sup> as evidenced by the narrow frequency range of OC<sub>i</sub> stretching modes in Table 3. From the calculated atomic displacements in Figure 10, the biring radical frequency with the largest OC<sub>i</sub> stretching contribution has a asymmetric contribution of OC<sub>i</sub> and C<sub>0</sub>C<sub>i</sub>/C<sub>0</sub>'C<sub>i</sub> stretching similar to that found with the 1530–1556 cm<sup>-1</sup> modes 19a of the Me-ImPhO<sup>-</sup> solvation models (Figure 7) and in agreement with the phenoxy radical solvation models.<sup>44</sup> However, the structural and vibrational inequality of the phenolic CC stretches due to the asymmetry in the phenoxy ring is clearly evidenced in the atomic displacements of Figure 10.

**1409–1439 cm<sup>-1</sup>, ν<sub>7a</sub>.** The calculated atomic displacements for the symmetric OC<sub>i</sub> and C<sub>0</sub>C<sub>i</sub>/C<sub>0</sub>'C<sub>i</sub> stretching mode 7a of

**TABLE 3:** Total Energy Decomposition (%) for Radical Stretching Frequencies

model	1r				1s			
$\nu$ (cm <sup>-1</sup> )	1479	1522	1537	1552	1466	1512	1529	1546
$E$ (Im) <sup>a</sup>	8	32	60	2	10	56	31	2
$E$ (PhO <sup>-</sup> ) <sup>b</sup>	60	52	32	95	42	34	62	93
$E$ (OC <sub>i</sub> ) <sup>c</sup>	5	34	13	23	1	22	37	13
$E$ (N <sub>e</sub> C <sub>0</sub> ) <sup>d</sup>	19	8	1	1	18	3	1	2
$E$ (CH <sub>3</sub> ) <sup>e</sup>	9	4	3	0	26	6	2	1
model	2r				2s			
$\nu$ (cm <sup>-1</sup> )	1479	1523	1541	1551	1487	1520	1535	1549
$E$ (Im) <sup>a</sup>	9	25	62	6	12	40	44	5
$E$ (PhO <sup>-</sup> ) <sup>b</sup>	58	64	31	89	39	49	50	91
$E$ (OC <sub>i</sub> ) <sup>c</sup>	0	44	11	15	1	33	24	13
$E$ (N <sub>e</sub> C <sub>0</sub> ) <sup>d</sup>	15	5	0	3	12	2	1	3
$E$ (CH <sub>3</sub> ) <sup>e</sup>	17	3	3	0	35	4	2	1
model	5r				5s			
$\nu$ (cm <sup>-1</sup> )	1471	1520	1536	1546	1475	1518	1533	1549
$E$ (Im) <sup>a</sup>	9	16	70	7	4	38	48	4
$E$ (PhO <sup>-</sup> ) <sup>b</sup>	65	66	22	90	32	50	45	92
$E$ (OC <sub>i</sub> ) <sup>c</sup>	6	47	5	17	1	36	22	11
$E$ (N <sub>e</sub> C <sub>0</sub> ) <sup>d</sup>	17	9	0	2	9	4	1	2
$E$ (CH <sub>3</sub> ) <sup>e</sup>	4	5	4	1	52	5	3	1

<sup>a</sup> The total energy contributed by imidazole. <sup>b</sup> The total energy contributed by phenoxyl radical. <sup>c</sup> The energy contributed by the OC<sub>i</sub> stretch. <sup>d</sup> The energy contributed by the N<sub>e</sub>C<sub>0</sub> stretch. <sup>e</sup> The energy contributed by the methyl group of imidazole.

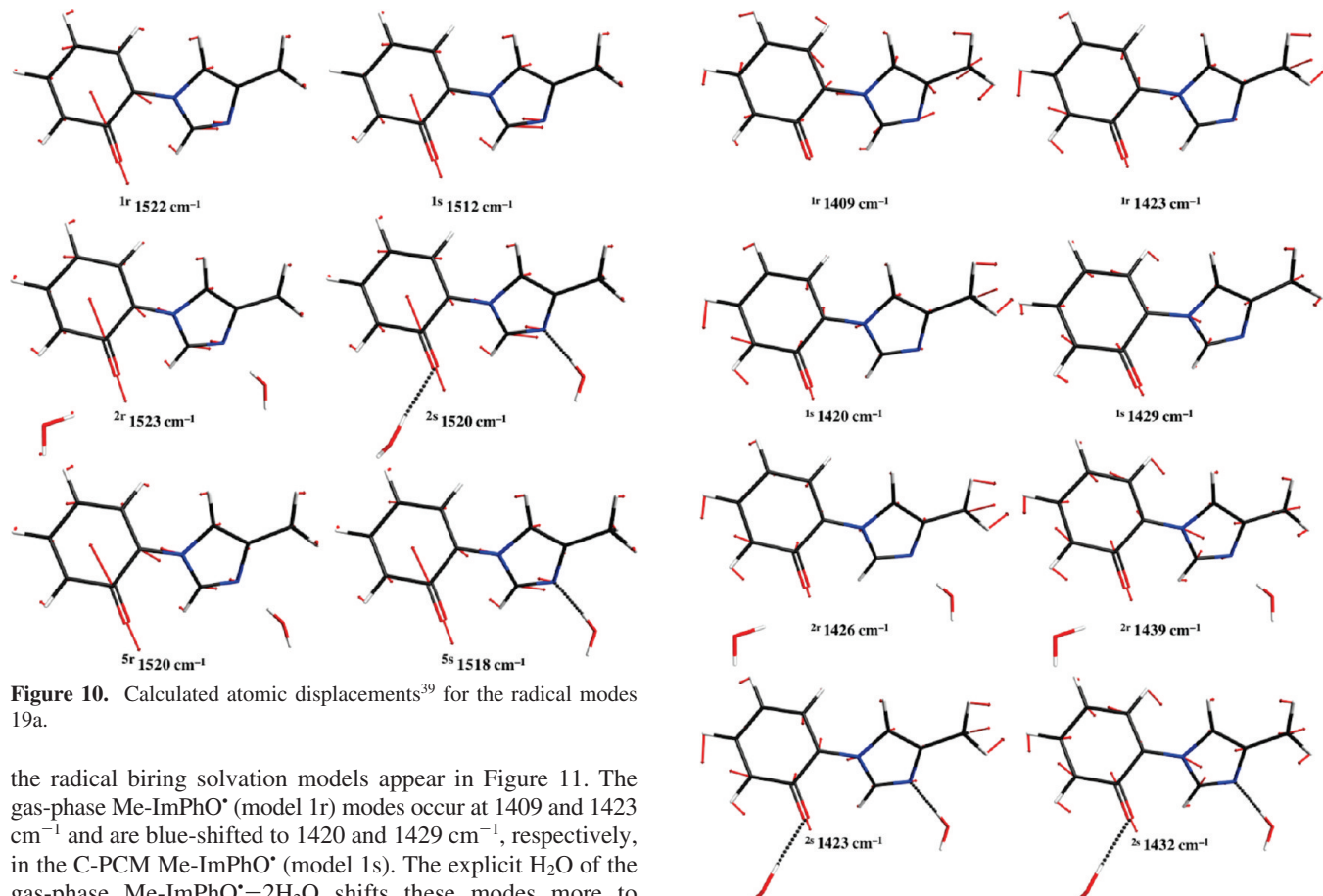


**Figure 10.** Calculated atomic displacements<sup>39</sup> for the radical modes 19a.

the radical biring solvation models appear in Figure 11. The gas-phase Me-ImPhO<sup>•</sup> (model 1r) modes occur at 1409 and 1423 cm<sup>-1</sup> and are blue-shifted to 1420 and 1429 cm<sup>-1</sup>, respectively, in the C-PCM Me-ImPhO<sup>•</sup> (model 1s). The explicit H<sub>2</sub>O of the gas-phase Me-ImPhO<sup>•</sup>-2H<sub>2</sub>O shifts these modes more to the blue than the addition of the C-PCM-water alone, and for the gas-phase Me-ImPhO<sup>•</sup>-2H<sub>2</sub>O (model 2r), these modes are calculated to be at 1426 and 1439 cm<sup>-1</sup>. The perturbation to the frequencies due to the C-PCM-water and explicit H<sub>2</sub>O is nonadditive, and the symmetric OC<sub>i</sub> and C<sub>0</sub>C<sub>i</sub>/C<sub>0</sub>'C<sub>i</sub> modes for model 2s are at 1423 and 1432 cm<sup>-1</sup>, between the C-PCM Me-ImPhO<sup>•</sup> (model 1s) and gas-phase Me-ImPhO<sup>•</sup>-2H<sub>2</sub>O (model 2r). However, for the Me-ImPhO<sup>•</sup> solvation models, the total energy

**Figure 11.** Calculated atomic displacements<sup>39</sup> for radical OC<sub>i</sub> stretching modes 7a.

contributed by the OC<sub>i</sub> stretch is 10% or less (data not shown), and these vibrations have no predicted intensity (Figure 9).

**Electronic Absorption Spectra, Singlet-State Models: Me-ImPhO<sup>•</sup> and Me-ImPhOH.** The TD-B3LYP/def2TZVPP(+)//B3LYP/6-31+G(d,p) spectra for the gas-phase anionic models

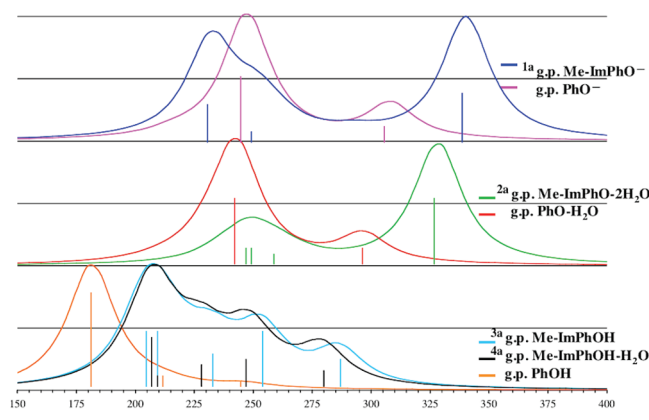


**Figure 12.** Gas-phase TD-RB3LYP/def2TZVPP(+)//RB3LYP/6-31+G(d,p) calculated spectra.

1a and 2a and neutral models 3a and 4a are presented in Figure 12, with the gas-phase phenolate anion, phenolate-H<sub>2</sub>O complex, and phenol spectra calculated at the same level of theory. The transition energies, oscillator strengths, and dominant configurations in the time-dependent expansion are presented in Table 4A for the phenol models and in Table 4B for the biring models.

The principal Kohn–Sham orbitals of the phenolate anion, phenolate-H<sub>2</sub>O complex, Me-ImPhO<sup>-</sup>, and Me-ImPhO-2H<sub>2</sub>O

appear in Figure 13. It is interesting to note that from the data in Table 4B and the MOs of Figure 13, the 251 nm transition in the gas-phase Me-ImPhO<sup>-</sup> spectrum is largely the oxygen lone-pair HOMO-1-*n* to LUMO+2- $\pi^*$  transition, and this transition has appreciable predicted intensity only in the gas-phase Me-ImPhO<sup>-</sup> spectrum.

The Kohn–Sham orbitals for Me-ImPhOH, Me-ImPhOH-H<sub>2</sub>O, and phenol are presented in Figure 14. The amplitudes over the phenol moiety for the LUMO and LUMO+1 of Me-ImPhOH, Me-ImPhOH-H<sub>2</sub>O, and phenol are similar, whereas the biring HOMO, HOMO-1, and HOMO-2 have significant amplitude over the imidazole ring, and in fact, these biring MOs are dominated by imidazole, with Mulliken populations of 1.722 and 1.700  $e^-$ , respectively, suggesting that the 286 and 279 nm HOMO-to-LUMO transitions of Me-ImPhOH and Me-ImPhOH-H<sub>2</sub>O, respectively, are best described as imidazole-to-phenol charge-transfer excitations.

**Radical Models.** The TD-UB3LYP/TZVPP(+)//UB3LYP/6-31+G(d,p) calculated spectra for the gas-phase Me-ImPhO<sup>•</sup>, Me-ImPhO<sup>•</sup>-H<sub>2</sub>O, and Me-ImPhO<sup>•</sup>-2H<sub>2</sub>O are presented in Figure 15, with the spectra for the gas-phase phenoxy radical and phenoxy-H<sub>2</sub>O radical complex calculated at the same level of theory. The absorption energies, oscillator strengths, and dominant configurations in the time-dependent expansion are presented in Table 5, and the Kohn–Sham  $\beta$ -spin orbitals are presented in Figure 16. As is observed with Me-ImPhOH and

**TABLE 4**

(A) Gas-Phase TDB3LYP Transition Energies, Oscillator Strengths, and Configurations							
	$f^a$	configuration <sup>b</sup>	weight, %		$f^a$	configuration <sup>b</sup>	weight, %
PhO <sup>-</sup>							
308 nm	0.057	0, 0	84	246 nm	0.033	0, 0	76
247 nm	0.207	0, 2	73	212 nm	0.030	1, 1	23
		2, 0	10			0, 1	59
PhO-H <sub>2</sub> O							
297 nm	0.054	0, 0	84	182 nm	0.373	1, 1	60
243 nm	0.226	0, 2	70	182 nm	0.592	1, 0	48
		2, 0	11			0, 1	21
(B) Gas-Phase TDB3LYP Transition Energies, Oscillator Strengths, and Configurations							
	$f^a$	configuration <sup>b</sup>	weight, %		$f^a$	configuration <sup>b</sup>	weight, %
<sup>1a</sup> Me-ImPhO <sup>-</sup>							
340 nm	0.167	0, 0	86	328 nm	0.164	0, 0	87
251 nm	0.029	1, 2	45	259 nm	0.017	0, 4	33
		2, 0	16			0, 3	26
		0, 2	14			0, 2	18
232 nm	0.132	2, 0	43	249 nm	0.022	0, 5	61
		3, 0	29			0, 3	14
				247 nm	0.021	2, 0	13
						0, 6	65
						2, 0	20
<sup>3a</sup> Me-ImPhOH							
286 nm	0.075	0, 0	92	279 nm	0.068	0, 0	92
253 nm	0.109	1, 0	49	248 nm	0.094	0, 1	54
		0, 1	34			1, 0	31
233 nm	0.074	2, 0	42	228 nm	0.075	1, 1	37
		1, 1	40			2, 0	29
212 nm	0.095	2, 0	31	206 nm	0.163	3, 0	14
		1, 1	30			0, 3	28
		0, 3	10			1, 1	22
204 nm	0.124	0, 3	29			0, 4	11
		2, 1	19			5, 0	10
		1, 3	12				
		3, 1	10				

<sup>a</sup> oscillator strength (in a.u.). <sup>b</sup> the dominant configuration in the time-dependent expansion: the format '*m,n*' counts from the HOMO downward (HOMO - *m*), and the LUMO upward (LUMO + *n*).

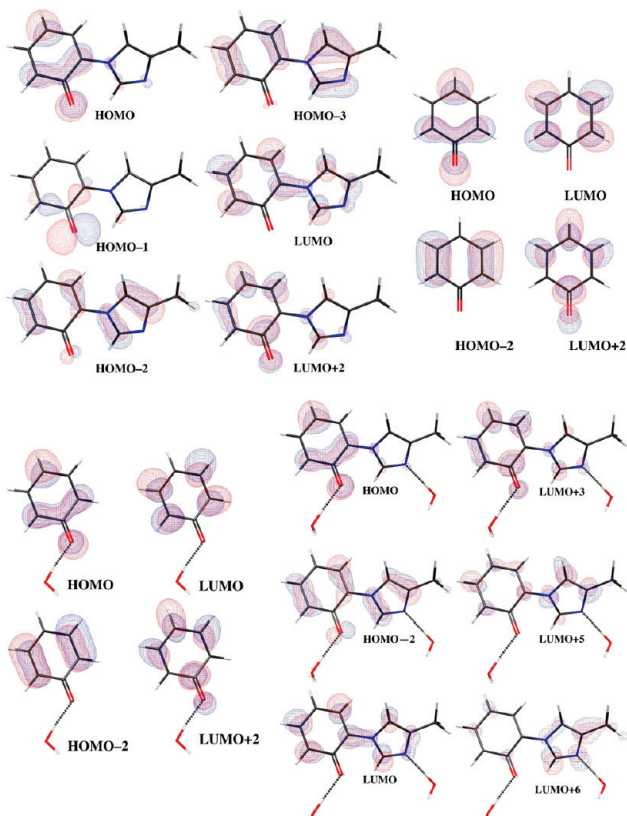


**Figure 13.** The Kohn–Sham orbitals<sup>39</sup> of Me-ImPhO<sup>-</sup> (upper left), phenolate anion (upper right), phenolate–H<sub>2</sub>O (lower left) and Me-ImPhO<sup>-</sup>–2H<sub>2</sub>O (lower right); isodensity = 0.01 au.

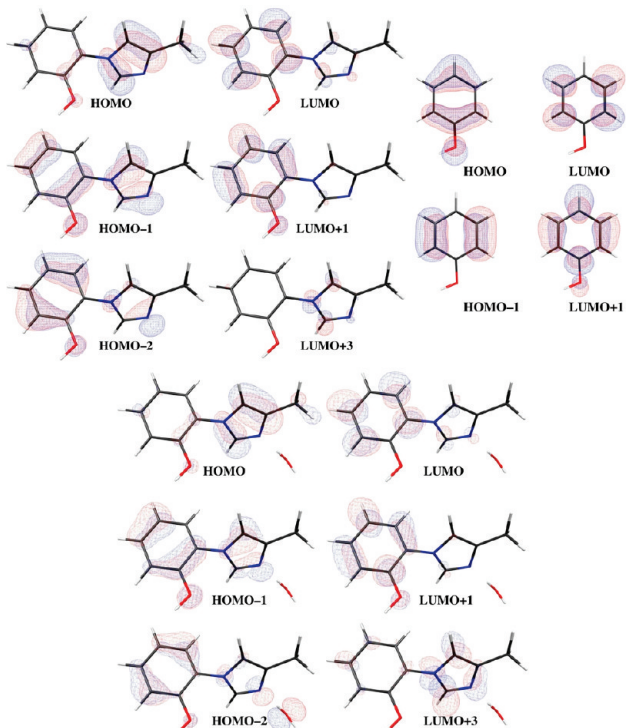


**Figure 14.** The Kohn–Sham orbitals<sup>39</sup> for Me-ImPhOH (upper left), phenol (upper right), and Me-ImPhOH–H<sub>2</sub>O (lower center); isodensity = 0.01 au.

Me-ImPhOH–H<sub>2</sub>O, the HOMO and HOMO-1 of the biring radicals have amplitude over the imidazole moiety (0.318, 0.237, and 0.268 e<sup>-</sup> for Me-ImPhO<sup>•</sup>, Me-ImPhO<sup>•</sup>–H<sub>2</sub>O, and Me-ImPhO<sup>•</sup>–2H<sub>2</sub>O, respectively), and consequently, the 617, 606,

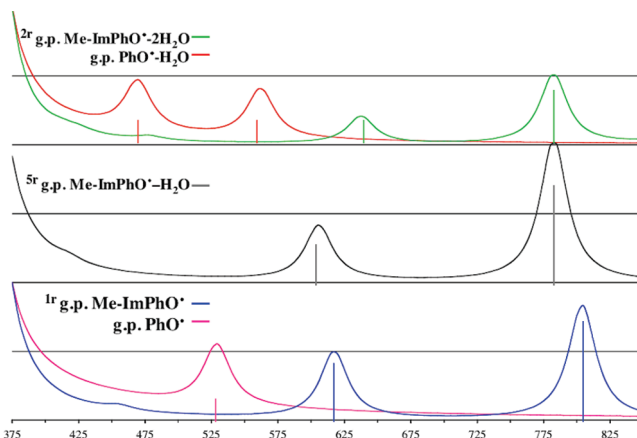


**Figure 15.** TD-UB3LYP/def2TZVPP(+)//UB3LYP/6-31+G(d,p) calculated spectra.

and 638 nm transitions of the Me-ImPhO<sup>•</sup>, Me-ImPhO<sup>•</sup>–H<sub>2</sub>O, and Me-ImPhO<sup>•</sup>–2H<sub>2</sub>O, respectively, have some imidazole-to-phenoxyl charge transfer character.

**Thermodynamic Properties.  $\Delta pK_a$ .** The  $pK_a$  of the phenolic–OH for the biring models was calculated relative to unmodified phenol using the isodesmic reactions of Scheme 1. The calculated reaction energies and the  $\Delta pK_a$  values are presented in Table 6. It is clear that for all of the reactions, the imidazole moiety of the biring models stabilizes the anion compared to unmodified phenol, increasing the acidity of the phenolic–OH. It is also clear that the calculated  $\Delta pK_a$  values are strongly solvation-dependent. For reactions A and B in the gas phase (Scheme 1), the calculated  $\Delta pK_a$  values are 5 times larger than experimental values for model compounds (Table 6).<sup>20–22,25</sup> Furthermore, the explicit H<sub>2</sub>O molecules in the gas-phase reaction B predict a  $\Delta pK_a$  that is more negative than that of the gas-phase reaction A. In contrast, the C-PCM-water-solvated reactions predict much smaller reaction energies, and the  $\Delta pK_a$  values are in reasonable agreement with experiment. Due to the small size of the phenolate anion and phenolate–H<sub>2</sub>O complex compared to Me-ImPhO<sup>-</sup> and Me-ImPhO<sup>-</sup>–2H<sub>2</sub>O, the gas-phase-to-solvent energy changes for phenolate and phenolate–H<sub>2</sub>O are slightly larger than that for Me-ImPhO<sup>-</sup> and Me-ImPhO<sup>-</sup>–2H<sub>2</sub>O (−60 and −57 kcal/mol vs −54 and −52 kcal/mol, respectively); however, the solvation energies for the anions are compensated by the larger gas-phase-to-solvent energy change of Me-ImPhOH and Me-ImPhOH–H<sub>2</sub>O compared to phenol (−10 and −13 kcal/mol vs −5 kcal/mol, respectively), resulting in a positive gas-phase-to-solvent reaction energy change and the small overall reaction energies for the C-PCM-water-solvated reactions A and B.

The calculated reaction energy of −13.41 kcal/mol for the gas-phase reaction A (Scheme 1, Table 6) is in reasonable agreement with other similar calculations.<sup>20,28,29</sup> Bu and Cukier<sup>28</sup> calculated the gas-phase proton dissociation energy for Me-ImCrOH to be −13.7 kcal/mol relative to *para*-cresol, in good agreement with the −14.9 kcal/mol gas-phase proton affinity of ImPhOH obtained by the van der Donk group.<sup>20</sup> Colbran and Paddon-Row<sup>29</sup> used an isodesmic reaction with the SCRF<sup>48</sup> solvation model and a dielectric constant of 4 to calculate the −26.8 kJ/mol (−6.41 kcal/mol) proton transfer energy of ImPhOH relative to phenol and obtained a  $\Delta pK_a$  of −4.7. This  $\Delta pK_a$  lies between the −9.83 obtained in the gas phase and the −2.50 obtained in the high-dielectric aqueous environment (reaction A, Table 6) as is to be expected. However, the observation that explicit H<sub>2</sub>O in the gas phase increases the

**TABLE 5:** Gas-Phase TDB3LYP/TZVPP(+) Transition Energies, Oscillator Strengths, and Configurations

	$f^a$	configuration <sup>b</sup>	weight, %		$f^a$	configuration <sup>b</sup>	weight, %
PhO <sup>•</sup>							
529 nm	0.005	1 $\beta$ , 0 $\beta$	99.7	562 nm	0.004	2 $\beta$ , 0 $\beta$	99
Me-ImPhO <sup>•</sup>							
804 nm	0.024	0 $\beta$ , 0 $\beta$	79	469 nm	0.004	1 $\beta$ , 0 $\beta$	98
617 nm	0.014	2 $\beta$ , 0 $\beta$	10	783 nm	0.026	0 $\beta$ , 0 $\beta$	77
		1 $\beta$ , 0 $\beta$	65	606 nm	0.010	1 $\beta$ , 0 $\beta$	11
		2 $\beta$ , 0 $\beta$	31			3 $\beta$ , 0 $\beta$	48
Me-ImPhO <sup>•</sup> -H <sub>2</sub> O							
895 nm	0.013	0 $\beta$ , 0 $\beta$	64			1 $\beta$ , 0 $\beta$	48
782 nm	0.018	3 $\beta$ , 0 $\beta$	32			0 $\beta$ , 0 $\beta$	48
		3 $\beta$ , 0 $\beta$	49			1 $\beta$ , 0 $\beta$	11
		0 $\beta$ , 0 $\beta$	32			1 $\beta$ , 0 $\beta$	77
		1 $\beta$ , 0 $\beta$	12			3 $\beta$ , 0 $\beta$	48
638 nm	0.007	1 $\beta$ , 0 $\beta$	62				
		3 $\beta$ , 0 $\beta$	18				

<sup>a</sup> Oscillator strength (in a.u.). <sup>b</sup> The dominant configuration in the time-dependent expansion: the format “ $m,n$ ” counts from the HOMO upward (i.e., HOMO –  $m$ ), and the LUMO downward (i.e., LUMO +  $n$ ); “ $\alpha$ ” and “ $\beta$ ” denote spin-up or spin-down orbitals, respectively.

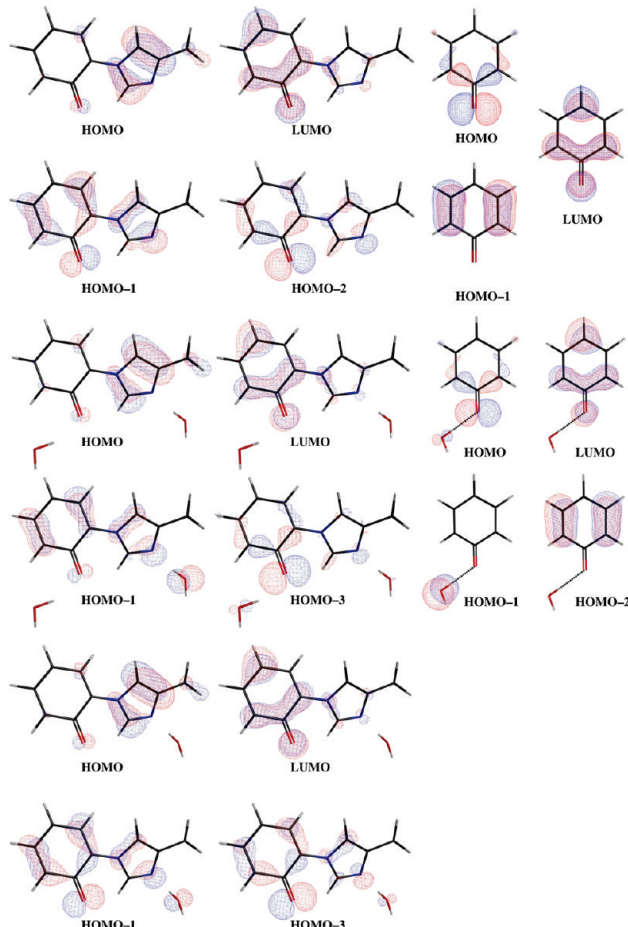


**Figure 16.** The Kohn–Sham  $\beta$ -spin orbitals<sup>39</sup> for Me-ImPhO<sup>•</sup> (upper left), phenoxy radical (upper right), Me-ImPhO<sup>•</sup>-2H<sub>2</sub>O (center left), PhO<sup>•</sup>-H<sub>2</sub>O (center right), and Me-ImPhO<sup>•</sup>-H<sub>2</sub>O (lower left); isodensity = 0.01 au.

acidity of the phenolic-OH suggests that the  $pK_a$  for the biring structure in the enzyme may be downshifted by more than 5 units compared to unmodified tyrosine and illustrates the sensitivity of the  $pK_a$  to environmental effects and to H-bonding interactions specifically.

**Anodic Redox Potential,  $\Delta\Phi$ .** The anodic redox potential for the biring radical/anion couple was calculated relative to

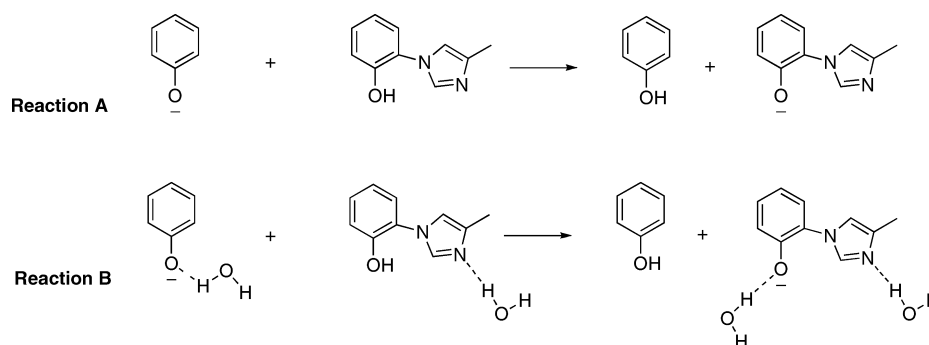
the phenolate anion/phenoxy radical using the isodesmic reactions in Scheme 2. The reaction energies and calculated potentials are presented in Table 7. As with the  $\Delta pK_a$  calculations, the gas-phase reaction energies predict potentials that are ~5 times larger than experiment, whereas the C-PCM-water-solvated reaction energies predict reaction potentials in reasonable agreement with experiment. For the C-PCM-water-solvated reaction C, the calculated potentials of +0.117 and +0.116 V are in excellent agreement with the 0.11 V from experiment (Table 7).<sup>26</sup>

The calculated gas-phase energy of -9.88 kcal/mol for reaction A in Scheme 2 is in good agreement with the +10.5 kcal/mol gas-phase electron affinity of the *para*-cresol radical relative to the Me-ImCrO<sup>•</sup>28 and the +10.9 kcal/mol gas-phase electron affinity of the phenoxy radical relative to the ImPhO<sup>•</sup> model.<sup>20</sup> By subtracting the reaction energy of B from that of C, one obtains the biring phenoxyl-O-H<sub>2</sub>O binding energy. It is clear that the H<sub>2</sub>O molecule at the phenolic-O further destabilizes Me-ImPhO<sup>•</sup>-2H<sub>2</sub>O by 1 kcal/mol relative to PhO<sup>•</sup>-H<sub>2</sub>O both in the gas phase and in C-PCM-water, illustrating the importance of the H-bonding interactions for the biring radical.

**ΔBDE.** The O–H bond dissociation energy for Me-ImPhOH was calculated relative to phenol using the isodesmic reactions in Scheme 3. The calculated energies are presented in Table 8. It is clear that the O–H bond of the biring model is slightly weakened relative to that in phenol; however, with solvation of the biring radical, the ΔBDE becomes more positive, demonstrating the destabilizing effects of the H<sub>2</sub>O on the biring radical. The -0.46 kcal/mol ΔBDE for the C-PCM-water-solvated reaction C in Table 8 is in good agreement with the -0.3 kcal/mol O–H ΔBDE of the van der Donk group,<sup>20</sup> calculated using the experimental  $pK_a$  and the anodic potential of ImPhOH,<sup>49</sup> and clearly demonstrates the need to include specific H-bonding interactions in solvation models of the biring radical.

## Discussion and Conclusions

In the present work, the effects of aqueous solvation on the physicochemical properties of Me-ImPhOH, a model of the cross-linked histidine–tyrosine ligand to Cu<sub>B</sub> in CcO, were investigated. Specific H-bonding solute–solvent interactions were separated from the bulk electrostatic interactions by

SCHEME 1:  $\Delta pK_a \approx \Delta E/2.303RT$ TABLE 6: Reaction Energies and  $\Delta pK_a$  Values for the Reactions in Scheme 1

reaction	phase	density functional	$\Delta E_R$ (kcal/mol)	$\Delta pK_a^a$
A	gas phase	B3LYP	-13.41	-9.83
	C-PCM-water	B3LYP	-3.41	-2.50
B	gas phase	B3LYP	-15.23	-11.18
	gas phase	PBE0	-16.23	-11.89
	C-PCM-water	B3LYP	-3.48	-2.55
C	C-PCM-water	PBE0	-3.21	-2.35
	experiment			-1.1, <sup>b</sup> -1.4, <sup>c</sup> -1.8 <sup>d</sup>

<sup>a</sup> Calculated from the reaction energy using  $\Delta pK_a = \Delta E_R (2.303RT)^{-1}$ . <sup>b</sup> Ref 22; the shift in the  $pK_a$  relative to *para*-cresol.

<sup>c</sup> Ref 20; the shift in the  $pK_a$  relative to phenol. <sup>d</sup> Ref 25; the shift in the  $pK_a$  relative to tyrosine.

comparing properties computed with C-PCM-water alone and in combination with models that include explicit  $H_2O$  molecules H-bonded to the phenolic-O and the  $N_\delta$  of imidazole. The computed properties include the structures and the vibrational and UV/visible spectra of the  $Me\text{-ImPhO}^-$  anion, the neutral  $Me\text{-ImPhOH}$ , and the neutral  $Me\text{-ImPhO}^\bullet$  radical solvation models. Additionally, the  $pK_a$ , the anodic redox potential, and the O–H bond-dissociation energy of the biring models were computed relative to the phenol/phenoxyl radical using a series of isodesmic reactions.

For the  $Me\text{-ImPhO}^-$  models, solvation most strongly perturbs the  $OC_i$  and  $C_0C_i/C_0'C_i$  bonds of the phenolate moiety, whereas the neutral  $Me\text{-ImPhOH}$  solvation model  $C_1N_e$  and  $N_\delta C_1$  bonds are most strongly affected by solvation. Because solvation is included, the biring anionic  $OC_i$  bond is lengthened 0.030 Å, similar to the 0.035 Å increase observed with unmodified phenolate anion solvation models.<sup>44</sup> For the neutral doublet biring radical, the  $OC_i$  bond is 0.006 Å shorter than in the

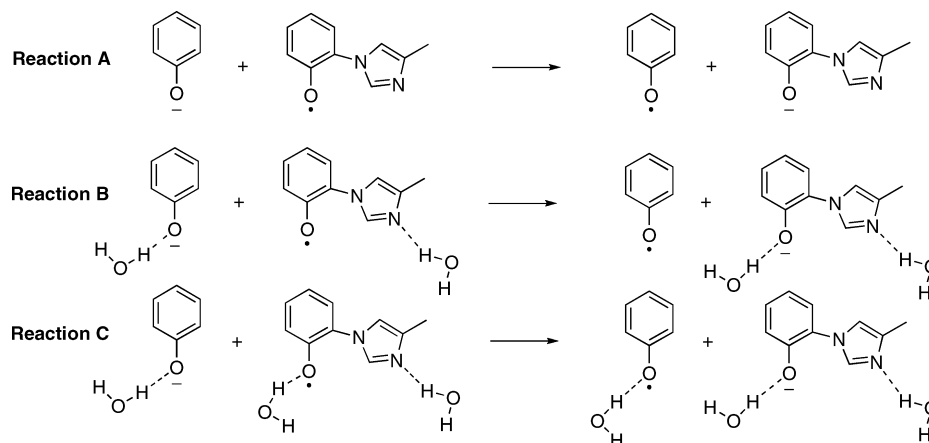
TABLE 7: Reaction Energies and Oxidation Potentials,  $\Delta\Phi$ , for the Reactions in Scheme 2

reaction	phase	density functional	$\Delta E_R$ (kcal/mol)	$\Delta\Phi$ (V) <sup>a</sup>
A	gas phase	B3LYP	-9.88	+0.429
	C-PCM-water	B3LYP	-1.21	+0.052
B	gas phase	B3LYP	-11.78	+0.511
	gas phase	PBE0	-13.36	+0.579
	C-PCM-water	B3LYP	-1.37	+0.059
C	C-PCM-water	PBE0	-1.50	+0.065
	gas phase	B3LYP	-12.94	+0.561
	gas phase	PBE0	-13.83	+0.600
D	C-PCM-water	B3LYP	-2.69	+0.117
	C-PCM-water	PBE0	-2.67	+0.116
	experiment			+0.07, <sup>b</sup> +0.11 <sup>c</sup>

<sup>a</sup> Calculated from the reaction energy using  $\Delta\Phi = \Delta E_R/F$ , where  $F$  is the Faraday constant. <sup>b</sup> Ref 21; anodic potential relative to *para*-cresol. <sup>c</sup> Ref 26; anodic potential relative to tyrosine.

phenoxy radical solvation models.<sup>44</sup> Furthermore, the biring radical  $OC_i$  bond is 0.01–0.04 Å shorter than in the biring anions, and a consistent 0.11 Å shorter than in the corresponding singlet neutral  $Me\text{-ImPhOH}$  solvation models. For the  $Me\text{-ImPhOH}$  solvation models, the  $N_e C_0$  bond is lengthened 0.008 Å with the inclusion of solvent, similar to the 0.007 Å increase observed in the biring radical solvation models. However, this bond is unchanged with inclusion of solvent for the biring anions.

For all of the singlet state models (anionic and neutral), solvation increases the  $C_1N_eC_0C_i$  torsion angle ~12°; however, the torsion angle of the singlet state neutral models is consistently 15° wider than that of the corresponding anionic model. The narrow torsion angles of the gas-phase  $Me\text{-ImPhO}^-$  and gas-phase  $Me\text{-ImPhO}-2H_2O$  suggest delocalization of the

SCHEME 2:  $\Delta\Phi \approx -\Delta E/F$ ,  $F$  = Faraday Constant

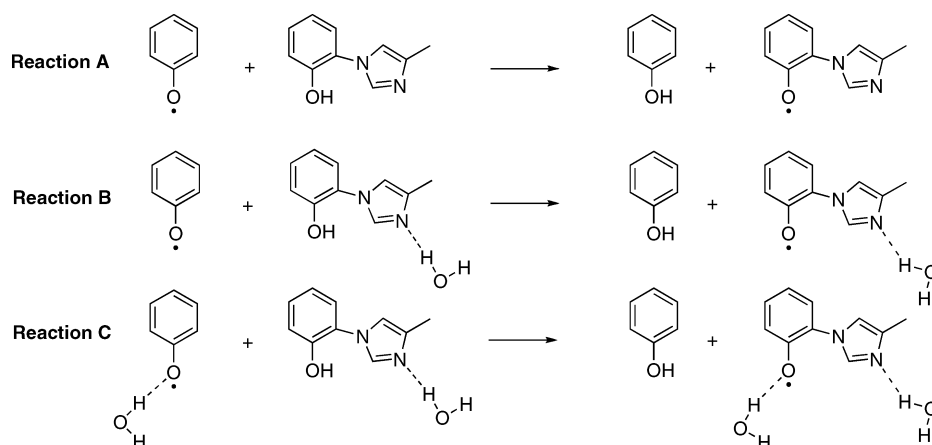
SCHEME 3: O–H Bond Dissociation Energy ( $\Delta\text{BDE}$ )

TABLE 8: O–H Bond Dissociation Energies (BDE) for the Reactions in Scheme 3

reaction	phase	density functional	$\Delta\text{BDE}$ (kcal/mol)
A	gas phase	B3LYP	-3.58
	C-PCM-water	B3LYP	-2.15
B	gas phase	B3LYP	-3.40
	gas phase	PBE0	-2.95
	C-PCM-water	B3LYP	-2.74
C	C-PCM-water	PBE0	-1.82
	gas phase	B3LYP	-2.31
	gas phase	PBE0	-1.95
	C-PCM-water	B3LYP	-1.32
	C-PCM-water	PBE0	-0.46

negative charge into the phenol and imidazole rings, whereas the C-PCM-water localizes the negative charge onto the phenolic-O, resulting in widened  $\text{C}_1\text{N}_e\text{C}_0\text{C}_i$  torsion angles and decreased overlap between the phenol and imidazole  $\pi$ -electron systems. For the doublet neutral biring radical solvation models, the  $\text{C}_1\text{N}_e\text{C}_0\text{C}_i$  torsion angle is 27–34°, similar to the narrow angles of the gas-phase Me-ImPhO<sup>−</sup> and gas-phase Me-ImPhO–2H<sub>2</sub>O. However, in the biring radical structures, the  $\pi$ -bonds of the imidazole ring are localized compared to the unmodified methylimidazole<sup>50</sup> or the singlet neutral biring models, suggesting reduced aromaticity for the Me-ImPhO<sup>•</sup> solution structures. Furthermore, the imidazole moiety induces significant asymmetry into the structure of the biring radical phenol ring, where the  $\text{C}_0\text{C}_i$  and  $\text{C}_m\text{C}_0$  bonds are 0.02 Å longer, and the  $\text{C}_0'\text{C}_i$  and  $\text{C}_m'\text{C}_0'$  bonds are 0.01 Å shorter than in the corresponding phenoxy radical solvation model.<sup>44</sup>

The solvent-sensitive asymmetric  $\text{OC}_i$  and  $\text{C}_0\text{C}_i/\text{C}_0'\text{C}_i$  stretching mode 19a is predicted at 1530–1555 cm<sup>−1</sup> for the anionic Me-ImPhO<sup>−</sup> solvation models and at 1553–1559 cm<sup>−1</sup> for the neutral Me-ImPhOH models (Figure 6). For the neutral Me-ImPhO<sup>•</sup> solvation models, the asymmetric  $\text{OC}_i$  and  $\text{C}_0\text{C}_i/\text{C}_0'\text{C}_i$  stretching mode 19a appears at 1512–1523 cm<sup>−1</sup>. It is found that for the C-PCM-solvated Me-ImPhO<sup>−</sup> and Me-ImPhO–2H<sub>2</sub>O and all the neutral Me-ImPhOH models, the  $\text{N}_e\text{C}_0$  stretch contributes 10–12% of the total energy to mode 19a, whereas for the gas-phase Me-ImPhO<sup>−</sup> and gas-phase Me-ImPhO–2H<sub>2</sub>O, the  $\text{N}_e\text{C}_0$  stretch contributes only 4 and 6%, respectively (Table 1A and B); however, for the neutral biring radical, the  $\text{N}_e\text{C}_0$  stretch does not contribute to mode 19a but makes the largest energy contribution to modes in the range of 1466–1480 cm<sup>−1</sup> (Table 3).

In the difference FT-IR spectrum of His–PhOH at pH 11,<sup>25</sup> an absorption band at 1522 cm<sup>−1</sup> was tentatively assigned to

the His–PhO<sup>•</sup> C–O stretching frequency, in reasonable agreement with the 1530 cm<sup>−1</sup> band observed in the UV resonance Raman spectrum of ImCrO<sup>•</sup>.<sup>22</sup> These frequencies are consistent with the ~1520 cm<sup>−1</sup> band observed in the  $\mathbf{P}_M$ -minus- $\mathbf{O}$  ATR-FTIR difference spectrum of the *P. denitrificans* CcO and possibly attributable to the cross-linked histidine–tyrosyl radical.<sup>17–19</sup> In the present work, the gas-phase Me-ImPhO<sup>•</sup> frequency with the largest  $\text{OC}_i$  contribution is fortuitously predicted at 1522 cm<sup>−1</sup>. With the inclusion of C-PCM-water, the  $\text{OC}_i$  stretch is blue-shifted, as is observed with the phenoxy radical,<sup>44</sup> and the  $\text{OC}_i$  stretch makes the largest energy contribution to the 1529 cm<sup>−1</sup> mode of the C-PCM-water-solvated Me-ImPhO<sup>•</sup> (model 1s). The explicit H<sub>2</sub>O H-bonded to the phenolic-O in the gas-phase model 2r provides a negligible 1 cm<sup>−1</sup> blue shift in this vibrational frequency. The consistent correlation of vibrational frequencies in the experimental and computed spectra of cross-linked radicals provides support for the generation of a tyrosyl radical in the  $\mathbf{P}_M$  intermediate.

The symmetric  $\text{OC}_i$  and  $\text{C}_0\text{C}_i/\text{C}_0'\text{C}_i$  stretching mode 7a is predicted to be at 1360–1407 cm<sup>−1</sup> for the biring anionic solvation models and at 1280–1300 cm<sup>−1</sup> for the neutral Me-ImPhOH solvation models. However, for the C-PCM-water-solvated Me-ImPhO<sup>−</sup> and all of the Me-ImPhOH solvation models, the  $\text{OC}_i$  stretch contributes to two modes at 1374 and 1386 cm<sup>−1</sup> for the C-PCM-water-solvated Me-ImPhO<sup>−</sup> and at 1280 and 1300 cm<sup>−1</sup> for the neutral models. In the FT-IR absorbance and FT-IR difference spectra of the cross-linked His–PhO<sup>−</sup> obtained in aqueous buffer at pH 11, two modes are observed at 1305 and 1265 cm<sup>−1</sup>.<sup>25</sup> The 1265 cm<sup>−1</sup> band is in close agreement with that observed in unmodified tyrosine,<sup>25,51</sup> and the band at 1305 cm<sup>−1</sup> is unique to the cross-linked His–PhOH and does not appear in the difference spectrum of tyrosine or the histidine–tyrosine dipeptide.<sup>25</sup> This 1305 cm<sup>−1</sup> His–PhO<sup>−</sup> absorbance band is in good agreement with a 1308 cm<sup>−1</sup> absorbance band assigned to the deprotonated cross-linked Y280 observed in the FT-IR spectra of the  $\mathbf{P}_R$  and  $\mathbf{F}$  intermediates from *P. denitrificans*.<sup>52,53</sup> The blue shift in the anionic biring OC<sub>i</sub> stretching frequency compared to unmodified tyrosinate is qualitatively reproduced here, although the predicted shifts are strongly solvation-dependent. For the gas-phase Me-ImPhO<sup>−</sup>, the OC<sub>i</sub> stretching frequency is only 8 cm<sup>−1</sup> higher in energy when compared to the gas-phase phenolate anion, whereas the gas-phase Me-ImPhO–2H<sub>2</sub>O frequency is shifted 50 cm<sup>−1</sup> to the blue compared to the gas-phase phenolate–H<sub>2</sub>O complex,<sup>44</sup> in reasonable agreement with the experimental 40 cm<sup>−1</sup> blue shift;<sup>25</sup> the C-PCM Me-ImPhO<sup>−</sup> and C-PCM Me-ImPhO–2H<sub>2</sub>O OC<sub>i</sub> stretching frequencies are 22 cm<sup>−1</sup> higher in energy than

the C-PCM-water-solvated phenolate and phenolate-H<sub>2</sub>O complex. These results illustrate the importance of including specific H-bonding interactions into computational models for the H-Y ligand.

For the Me-ImPhO<sup>•</sup> solvation models, the OC<sub>i</sub> stretch contributes to two modes separated by ~10 cm<sup>-1</sup>. The higher frequency mode at 1423–1440 cm<sup>-1</sup> is the symmetric OC<sub>i</sub> and C<sub>0</sub>C<sub>i</sub>/C<sub>0</sub>'C<sub>i</sub> stretching mode 7a; the lower frequency modes at 1410–1426 cm<sup>-1</sup> have asymmetric contributions from C<sub>0</sub>C<sub>i</sub> and C<sub>0</sub>'C<sub>i</sub> stretching (Figure 11) and reflect the structural and vibrational inequality of these bonds. However, for all the Me-ImPhO<sup>•</sup> solvation models, neither of these OC<sub>i</sub> stretching modes have predicted IR-absorbance intensity (Figure 9).

The gas-phase TD-RB3LYP/def2TZVPP(+)//RB3LYP/6-31+G(d,p) spectra predict HOMO-to-LUMO absorptions for the neutral Me-ImPhOH and Me-ImPhOH-H<sub>2</sub>O at 286 and 279 nm, respectively, in good agreement with the 280 nm absorption in the spectrum of His-PhOH.<sup>25</sup> However, there are many more transitions predicted at higher energy for these biring models, and the TD-B3LYP spectra are more complicated than the experimental His-PhOH spectrum.<sup>25</sup> The phenolate and phenolate-H<sub>2</sub>O HOMO-to-LUMO absorptions are red-shifted 62 and 51 nm relative to phenol, respectively, and the HOMO-to-LUMO transitions of Me-ImPhO<sup>•</sup> and Me-ImPhO-2H<sub>2</sub>O are red-shifted 54 and 49 nm compared to Me-ImPhOH and Me-ImPhOH-H<sub>2</sub>O, respectively. These shifts are in qualitative agreement with the 20 nm red-shift observed for *para*-cresolate compared to *para*-cresol and the 20 nm red shift observed for His-PhO<sup>•</sup> compared to His-PhOH.<sup>25</sup> An analysis of the Kohn-Sham orbitals suggests that for the gas-phase Me-ImPhO<sup>•</sup> and Me-ImPhO-2H<sub>2</sub>O anions, the occupied imidazole and phenolate orbitals overlap, but the energy ordering of the phenolate orbitals is unperturbed when compared to the phenolate anion and phenolate-H<sub>2</sub>O complex (Figure 13). Furthermore, the imidazole contribution to the biring LUMO increases the predicted absorption intensity of the HOMO-to-LUMO transition of the biring Me-ImPhO<sup>•</sup> and Me-ImPhO-2H<sub>2</sub>O relative to the phenolate anion and phenolate-H<sub>2</sub>O, in agreement with experiment (Table 4A and B).<sup>25</sup> The admixture of the imidazole π\* orbitals to the unoccupied orbitals may also account for the resonance enhancement of imidazole vibrational modes in the UVRR spectrum of ImCrOH.<sup>22</sup> For the Me-ImPhOH and Me-ImPhOH-H<sub>2</sub>O, the amplitudes of the HOMO and LUMO orbitals are significantly changed when compared to phenol (Figure 14), and the HOMO-to-LUMO transition of the neutral biring models is best described as an imidazole-to-phenol charge-transfer excitation.

In the electronic spectra of phenoxy<sup>54,55</sup> and *para*-cresol<sup>56</sup> radicals, an absorption is observed at 400 nm, similar to the 400 nm absorption in the time-resolved optical spectrum of the tyrosyl radical.<sup>25</sup> In the time-resolved optical spectrum of the His-PhO<sup>•</sup>, a unique absorption band appears at 500 nm, shifted 100 nm to the red of the unmodified tyrosyl radical spectrum.<sup>25</sup> In the TD-UB3LYP calculated spectra presented here (Figure 15), the Me-ImPhO<sup>•</sup> radical absorption at 617 nm is shifted 88 nm to the red of the 529 nm phenoxy radical absorption, in agreement with experiment; however, the absolute absorption energies of 529 and 617 nm for the phenoxy and Me-ImPhO<sup>•</sup> radicals, respectively, are 100 nm to the red of the experimental absorptions.<sup>25</sup> Upon inclusion of explicit H<sub>2</sub>O molecules, the phenoxy radical absorption is shifted to 562 nm, 33 nm to the red of the phenoxy radical. For the biring radicals, addition of the explicit H<sub>2</sub>O to the N<sub>δ</sub> of imidazole provides a modest 9 nm blue shift to the 617 nm Me-ImPhO<sup>•</sup> absorption,

whereas the H<sub>2</sub>O molecules at both the N<sub>δ</sub> and phenolic-O shift this absorption back to the red, and the 638 nm absorption of Me-ImPhO<sup>•</sup>-2H<sub>2</sub>O is an acceptable 78 nm to the red of the 562 nm phenoxy-H<sub>2</sub>O radical absorption. As was observed with the singlet-state neutral Me-ImPhOH and Me-ImPhOH-H<sub>2</sub>O orbitals, the biring radical HOMO-βπ and HOMO-1-βπ orbitals have amplitude over the imidazole moiety, and consequently, the HOMO-βπ-to-LUMO-βπ transitions have some imidazole-to-phenol charge-transfer character.

Using isodesmic reactions, the pK<sub>a</sub> of the phenolic-OH for Me-ImPhOH was calculated relative to phenol. It is found that the gas-phase reactions predict ΔpK<sub>a</sub> values that are 5 times larger than experiment,<sup>20–22,25</sup> and in the gas phase, the inclusion of explicit H<sub>2</sub>O molecules at the phenolic-O and N<sub>δ</sub> of the biring anion further increases the acidity of the phenolic-OH for the biring models relative to phenol. The C-PCM-water solvation greatly reduces the reaction energy, and the calculated ΔpK<sub>a</sub> of -2.35 obtained with the R-PBE0 hybrid functional and the C-PCM-water-solvated Me-ImPhOH-H<sub>2</sub>O and Me-ImPhO-2H<sub>2</sub>O models is in good agreement with the experimental ΔpK<sub>a</sub> of -1.1 to -1.8.<sup>20–22,25</sup> These results, combined with the calculated ΔpK<sub>a</sub> of -4.7 obtained with the SCRF and a low dielectric,<sup>29</sup> suggest that the pK<sub>a</sub> of the biring ligand in the inhomogeneous low-dielectric environment of the enzyme may be downshifted more than the experimental 1–2 log units obtained in aqueous solution, consistent with the proposed role of the H-Y ligand as a proton donor. Furthermore, given that the H-Y ligand is located at the terminus of the proton transfer K-channel<sup>3,4</sup> and the sensitivity of this property to environmental interactions, specific H-bonding partners should be included in reliable calculations of the thermodynamic properties of this novel ligand.

The anodic redox potential of the Me-ImPhO<sup>•</sup> solvation models was calculated relative to the phenolate/phenoxy radical using a series of isodesmic reactions. As was observed with the ΔpK<sub>a</sub> calculations, the gas-phase results are ~5 times larger than those observed experimentally, and the biring radical reduction potentials for the gas-phase reactions that include specific H-bonding interactions are larger than the potentials for reactions without H-bonding interactions.<sup>21,26</sup> Inclusion of the C-PCM-water solvent results in an order of magnitude decrease in the anodic redox potential for the biring radical, and the calculated potentials of +0.065 and +0.116 V obtained with the PBE0 hybrid functional and the C-PCM Me-ImPhO<sup>•</sup>-H<sub>2</sub>O and C-PCM Me-ImPhO<sup>•</sup>-2H<sub>2</sub>O radical solvation models, respectively, are in excellent agreement with the experimental values of +0.07 and +0.11 V.<sup>21,26</sup> These results suggest that the reduction potential for the biring radical may be significantly more positive than that of the tyrosyl radical in the inhomogeneous low dielectric environment of the membrane bound enzyme.

Isodesmic reactions were used to calculate the O-H BDE of the biring models relative to the phenol solvation models. For all the reactions, the biring O-H bond is weakened relative to phenol; however, the ΔBDEs are small in magnitude (<4 kcal/mol), and with the inclusion of solvent, the biring O-H ΔBDE becomes more positive, suggesting the O-H bond in the aqueous environment is not significantly weaker than that of the unmodified phenol. The -0.46 kcal/mol ΔBDE obtained with the PBE0 functional and the C-PCM-solvated Me-ImPhOH-H<sub>2</sub>O and Me-ImPhO<sup>•</sup>-2H<sub>2</sub>O models is in good agreement with the -0.30 kcal/mol obtained from the experimental ImPhOH pK<sub>a</sub> and anodic redox potential.<sup>54</sup>

The reaction of the mixed-valence CcO with dioxygen, a state that mimics the physiological conditions of limiting external reductant, produces the **P<sub>M</sub>** intermediate characterized by oxidized  $a_3^{3+}$ , oxidized Cu<sub>A</sub><sup>2+</sup>, oxoferryl  $a_3^{4+}=O^{2-}$ , oxidized Cu<sub>B</sub><sup>2+</sup>, and a putative Y\*. The one-electron-reduced state leading from **P<sub>M</sub>** to the **F** intermediate has been suggested to involve an equilibrium mixture of Cu(II):Y<sup>-</sup> and Cu(I):Y\*.<sup>57,58</sup> The populations and dynamics of this equilibrium depend sensitively on the relative reduction potentials of Cu(II)–OH, Cu(II)–H<sub>2</sub>O, and Y\*. Although the computational models of the present report lack copper, the order-of-magnitude decrease in the reduction potential of the biring radical ligand compared to the phenoxy radical upon inclusion of C-PCM-water and the 100 mV increase in the biring radical reduction potential upon inclusion of explicit H<sub>2</sub>O in the gas phase clearly demonstrate the sensitivity of this property to environmental interactions and the delicate fine-tuning of this property in the enzyme. Kaila et al. note that the reduction potential of the Cu<sub>B</sub> center is quite sensitive to a positive point charge modeling the lysine-319 (in the bovine numbering) of the K-channel located 10 Å from the tyrosine and that the Cu(II):Y<sup>-</sup> and Cu(I):Y\* equilibrium is shifted in favor of the Cu(II):Y<sup>-</sup> resonance form with the inclusion of this point charge.<sup>57</sup> Molecular dynamics simulations of the proton delivery K-channel have identified a persistent water molecule H-bonded to the hydroxyl of the cross-linked tyrosine and water chains H-bonded to the farnesyl chain of  $a_3$  that will effectively screen the positive charge of the lysine residue.<sup>59</sup> Given the sensitivity of the reduction potential of the biring radical, explicit consideration of the environment, and of H-bonding interactions specifically, is vital for the quantitative prediction of reaction energies and intermediate populations.

## Abbreviations

CcO = cytochrome *c* oxidase.

Cu<sub>A</sub> = binuclear copper A.

Cu<sub>B</sub> = mononuclear copper B.

*a* = low-spin heme *a*.

*a*<sub>3</sub> = high-spin heme *a*<sub>3</sub>.

H–Y = the cross-linked histidine–tyrosine copper B ligand.

His–PhOH = cross-linked histidine–phenol.

His–PhO<sup>•</sup> = cross-linked histidine–phenoxy radical.

ImPhOH = 2-(imidazole-1-yl)-phenol.

ImPhO<sup>-</sup> = 2-(imidazole-1-yl)-phenolate anion.

ImPhO<sup>•</sup> = 2-(imidazole-1-yl)-phenoxy radical.

ImCrOH = 2-(imidazol-1-yl)-4-methylphenol.

ImCrO<sup>-</sup> = 2-(imidazol-1-yl)-4-methylphenolate anion.

ImCrO<sup>•</sup> = 2-(imidazol-1-yl)-4-methylphenoxy radical.

Me-ImCrOH = 2-(4-methylimidazol-1-yl)-4-methylphenol.

Me-ImCrO<sup>-</sup> = 2-(4-methylimidazol-1-yl)-4-methylphenolate anion.

Me-ImCrO<sup>•</sup> = 2-(4-methylimidazol-1-yl)-4-methylphenoxy radical.

Me-ImPhOH = models 3a–b, 2-(4-methylimidazol-1-yl)-phenol.

Me-ImPhO<sup>-</sup> = models 1a–b, 2-(4-methylimidazol-1-yl)-phenolate anion.

Me-ImPhO<sup>•</sup> = models 1r–s, 2-(4-methylimidazol-1-yl)-phenoxy radical.

Me-ImPhOH–H<sub>2</sub>O = models 4a–b, 2-(4-methylimidazol-1-yl)-phenol with an H<sub>2</sub>O hydrogen bonded to the N<sub>δ</sub> of imidazole.

Me-ImPhO–2H<sub>2</sub>O = models 2a–b, 2-(4-methylimidazol-1-yl)-phenolate anion with an H<sub>2</sub>O hydrogen bonded to the N<sub>δ</sub> of imidazole and an H<sub>2</sub>O hydrogen bonded to the phenolic O.

Me-ImPhO<sup>•</sup>–H<sub>2</sub>O = models 5r–s, 2-(4-methylimidazol-1-yl)-phenoxy radical with an H<sub>2</sub>O hydrogen bonded to the N<sub>δ</sub> of imidazole.

Me-ImPhO<sup>•</sup>–2H<sub>2</sub>O = models 2r–s, 2-(4-methylimidazol-1-yl)-phenoxy radical with an H<sub>2</sub>O hydrogen bonded to the N<sub>δ</sub> of imidazole and an H<sub>2</sub>O hydrogen bonded to the phenolic O.

C-PCM = conductor-like polarizable continuum model.

TDB3LYP = time-dependent B3LYP.

BDE = bond dissociation energy.

**Acknowledgment.** This work was supported by the National Institutes of Health Grant GM53788.

## References and Notes

- Ferguson-Miller, S.; Babcock, G. T. *Chem. Rev.* **1996**, *96*, 2889–2907.
- Wikström, M. K. F. *Nature* **1977**, *266*, 271–273.
- Muramoto, K.; Hirata, K.; Shinzawa-Itoh, K.; Yoko-o, S.; Yamashita, E.; Aoyama, H.; Tsukihara, T.; Yoshikawa, S. *Proc. Natl. Acad. Sci. U.S.A.* **2007**, *104*, 7881–7886.
- Yoshikawa, S.; Shinzawa-Itoh, K.; Nakashima, R.; Yanoe, R.; Yamashita, E.; Inoue, N.; Yao, M.; Fei, M. J.; Libeu, C. P.; Mitzushima, T.; Yamaguchi, H.; Tomizaki, T.; Tsukihara, T. *Science* **1998**, *280*, 1723–1731.
- DeLano, W. L. *The PyMOL Molecular Graphics System*; Delano Scientific LLC: San Carlos, CA; <http://www.pymol.org>, PyMOLX11Hybrid V. 0.97.
- Brunori, M.; Giuffre, A.; Sarti, P. *J. Inorg. Biochem.* **2005**, *99*, 324–336.
- Morgan, J. E.; Verkhovsky, M. I.; Palmer, G.; Wikström, M. K. F. *Biochemistry* **2001**, *40*, 6882–6892.
- Blomberg, M. R. A.; Siegbahn, P. E. M.; Babcock, G. T.; Wikström, M. K. F. *J. Inorg. Biochem.* **2000**, *80*, 261–269.
- Proshlyakov, D. A.; Pressler, M. A.; Babcock, G. T. *Proc. Natl. Acad. Sci. U.S.A.* **1998**, *95*, 8020–8025.
- Proshlyakov, D. A.; Pressler, M. A.; DeMaso, C.; Leykam, J. F.; DeWitt, D. L.; Babcock, G. T. *Science* **2000**, *290*, 1588–1591.
- Sucheta, A.; Szundi, I.; Einarsdóttir, Ó. *Biochemistry* **1998**, *37*, 17905–17914.
- MacMillan, F.; Kannt, A.; Behr, J.; Prisnerk, R.; Michel, H. *Biochemistry* **1999**, *38*, 9179–9784.
- Svistunenko, D.; Wilson, M. T.; Cooper, C. E. *Biochim. Biophys. Acta* **2004**, *1655*, 372–380.
- Rigby, S. E. J.; Jüinemann, S.; Rich, P. R.; Heathcote, P. *Biochemistry* **2000**, *39*, 5921–5928.
- Budiman, K.; Kannt, A.; Lyubenova, S.; Richter, O.-M. H.; Ludwig, B.; Michel, H.; MacMillan, F. *Biochemistry* **2004**, *43*, 11709–11716.
- Berthomieu, C.; Hienerwadel, R. *Biochim. Biophys. Acta* **2005**, *1707*, 51–66.
- Iwaki, M.; Puustinen, A.; Wikström, M.; Rich, P. R. *Biochemistry* **2003**, *42*, 8809–8817.
- Iwaki, M.; Puustinen, A.; Wikström, M.; Rich, P. R. *Biochemistry* **2004**, *43*, 14370–14378.
- Iwaki, M.; Puustinen, A.; Wikström, M.; Rich, P. R. *Biochemistry* **2006**, *45*, 10873–10885.
- Pratt, D. A.; Pesavento, R. P.; van der Donk, W. A. *Org. Lett.* **2005**, *7*, 2735–2738.
- McCauley, K. M.; Vrtis, J. M.; Dupont, J.; van der Donk, W. A. *Org. Lett.* **2000**, *122*, 2403–2404.
- Aki, M.; Ogura, T.; Naruta, Y.; Le, T. H.; Sato, T.; Kitagawa, T. *J. Phys. Chem. A* **2002**, *106*, 3436–3444.
- Kim, S. H.; Aznar, C.; Brynda, M.; Silks, L. A.; Michalczyk, R.; Unkefer, C. J.; Woodruff, W. H.; Britt, R. D. *J. Am. Chem. Soc.* **2004**, *126*, 2328–2338.
- Elliott, G. I.; Konopelski, J. P. *Org. Lett.* **2000**, *2*, 3055–3057.
- Cappuccio, J. A.; Ayala, I.; Elliott, G. I.; Szundi, I.; Lewis, J.; Konopelski, J. P.; Barry, B. A.; Einarsdóttir, Ó. *J. Am. Chem. Soc.* **2002**, *124*, 1750–1760.
- Offenbacher, A.; White, K. N.; Sen, I.; Oliver, A. G.; Konopelski, J. P.; Barry, B. A.; Einarsdóttir, Ó. *J. Phys. Chem. B* **2009**, *113*, 7407–7417.
- Barone, V.; Cossi, M. *J. Phys. Chem. A* **1998**, *102*, 1995–2001.
- Bu, Y.; Cukier, R. I. *J. Phys. Chem. B* **2005**, *109*, 22013–22026.
- Colbran, S. B.; Paddon-Row, M. N. *J. Biol. Inorg. Chem.* **2003**, *8*, 855–865.
- Tomson, F.; Bailey, J. A.; Gennis, R. B.; Unkefer, C. J.; Li, Z.; Silks, L. A.; Martinez, R. A.; Donohoe, R. J.; Dyer, R. B.; Woodruff, W. H. *Biochemistry* **2002**, *41*, 14383–14390.
- Barone, V.; Cossi, M. *J. Phys. Chem. A* **1998**, *102*, 1995–2001.

- (32) Cossi, M.; Rega, N.; Salmani, G.; Barone, V. *J. Comput. Chem.* **2003**, *24*, 669–681.
- (33) Schmidt, M. W.; Baldridge, K. K.; Boatz, J. A.; Elbert, S. T.; Gordon, M. S.; Jensen, J. H.; Koseki, S.; Matsunaga, K.; Nguyen, K. A.; Su, S.; Windus, T. L.; Dupuis, M.; Montgomery, J. A., Jr. *J. Comput. Chem.* **1993**, *14*, 1347–1363.
- (34) Becke, A. D. *J. Chem. Phys.* **1993**, *98*, 5648–5642.
- (35) Stephens, P. J.; Devlin, F. J.; Chablowski, C. F.; Frisch, M. J. *J. Phys. Chem.* **1994**, *98*, 11623–11627.
- (36) Frisch, M. J.; Pople, J. A.; Binkley, J. S. *J. Chem. Phys.* **1984**, *80*, 3265–3269.
- (37) Schafer, A.; Horn, H.; Ahlrichs, R. *J. Chem. Phys.* **1992**, *97*, 2571–2577, Obtained via anonymous ftp from ftp://ftp.chemie.uni-karlsruhe.de/pub/basen.
- (38) Kendall, R. A.; Dunning, T. H., Jr.; Harrison, R. J. *J. Chem. Phys.* **1992**, *96*, 6796–6806.
- (39) Xu, X.; Goddard, W. A., III *Proc. Natl. Acad. Sci.* **2004**, *101*, 2673–2677.
- (40) Zhao, Y.; Truhlar, D. G. *J. Chem. Theory Comput.* **2005**, *1*, 415–432.
- (41) Santra, B.; Michaelides, A.; Scheffler, M. *J. Chem. Phys.* **2007**, *127*, 184104-1–184104-9.
- (42) Adamo, C.; Barone, V. *J. Chem. Phys.* **1999**, *110*, 6158–6170.
- (43) Figure generated using MacMolPlt 7.2.1. Bode, B. M.; Gordon, M. S. *J. Mol. Graphics Model.* **1998**, *16*, 133–138.
- (44) McDonald, W. J.; Einarsdóttir, Ó. *J. Phys. Chem. A* **2008**, *112*, 11400–11413.
- (45) Pulay, P.; Fogarasi, G.; Pang, F.; Boggs, J. E. *J. Am. Chem. Soc.* **1979**, *101*, 2550–2560. Fogarasi, G.; Zhou, X.; Taylor, P. W.; Pulay, P. *J. Am. Chem. Soc.* **1992**, *114*, 8191–8201.
- (46) Pulay, P.; Torok, F. *Acta Chim. Acad. Sci. Hung.* **1966**, *47*, 273–297.
- (47) Boatz, J. A.; Gordon, M. S. *J. Phys. Chem.* **1989**, *93*, 1819–1826.
- (48) Miertus, S.; Scrocco, E.; Tomasi, J. *Chem. Phys.* **1981**, *55*, 117–129. Cossi, M.; Barone, V.; Cammi, R.; Tomasi, J. *Chem. Phys. Lett.* **1996**, *255*, 327–335.
- (49) Bordwell, F. G.; Hausch, M. J. *J. Am. Chem. Soc.* **1986**, *108*, 1979–1985.
- (50) Toyama, A.; Ono, K.; Hashimoto, S.; Takeuchi, H. *J. Phys. Chem. A* **2002**, *106*, 3404–3412.
- (51) Range, K.; Ayala, I.; York, D.; Barry, B. A. *J. Phys. Chem. B* **2006**, *110*, 10970–10981.
- (52) Gorbikova, E. A.; Belevich, I.; Wikström, M.; Verkhovsky, M. I. *Proc. Natl. Acad. Sci. U.S.A.* **2008**, *105*, 10733–10737.
- (53) Gorbikova, E. A.; Wikström, M.; Verkhovsky, M. I. *J. Biol. Chem.* **2008**, *283*, 34907–34912.
- (54) Radziszewski, J. G.; Gill, M.; Gorski, A.; Spanget-Larsen, J.; Waluk, J.; Mróz, B. *J. Chem. Phys.* **2001**, *115*, 9733–9738.
- (55) Tripathy, G. N. R.; Schuler, R. H. *J. Chem. Phys.* **1984**, *84*, 113–121.
- (56) Tripathy, G. N. R.; Schuler, R. H. *J. Phys. Chem.* **1988**, *92*, 5129–5133.
- (57) Kaila, V. R. I.; Johansson, M. P.; Sundholm, D.; Laakkonen, L.; Wikström, M. *Biochim. Biophys. Acta* **2009**, *1787*, 221–233.
- (58) Lonnro, D. G.; Lee, S. T.; Colbran, S. B. *J. Am. Chem. Soc.* **2007**, *129*, 5800–5801.
- (59) Cukier, R. I. *Biochim. Biophys. Acta* **2005**, *1706*, 134–146.

JP909574V